Missouri S&T Library and Learning Resources

Scholars' Mine

Masters Theses

Student Theses and Dissertations

Summer 2018

Laser-aided additive manufacturing of glass

John Michael Hostetler

Follow this and additional works at: https://scholarsmine.mst.edu/masters_theses

Part of the Manufacturing Commons

Department:

Recommended Citation

Hostetler, John Michael, "Laser-aided additive manufacturing of glass" (2018). *Masters Theses*. 8077.
https://scholarsmine.mst.edu/masters_theses/8077

This thesis is brought to you by Scholars' Mine, a service of the Missouri S&T Library and Learning Resources. This work is protected by U. S. Copyright Law. Unauthorized use including reproduction for redistribution requires the permission of the copyright holder. For more information, please contact scholarsmine@mst.edu.

LASER-AIDED ADDITIVE MANUFACTURING OF GLASS

by

JOHN MICHAEL HOSTETLER

A THESIS

Presented to the Faculty of the Graduate School of the

MISSOURI UNIVERSITY OF SCIENCE AND TECHNOLOGY

In Partial Fulfillment of the Requirements for the Degree

MASTER OF SCIENCE IN MECHANICAL ENGINEERING

2018

Approved by:

Edward C. Kinzel, Advisor
Douglas A. Bristow
Robert G. Landers

ABSTRACT

This thesis presents various approaches for the laser-aided additive manufacturing of glass. First, a technique is investigated to create free-form, low to zero coefficient of thermal expansion structures out of silica-gel. A CO_2 laser was coupled through a gantry system and focused onto a binder-free silica-gel powder bed (15-40 μm particles). Prior to writing each layer, powder is dispensed by sifting it onto the build platform as opposed to a conventional wiper system, avoiding contacting and potentially damaging sensitive parts. After deposition, the parts are annealed in a furnace to increase their strength. The influence of various process parameters including scan speed and laser power on final shape is investigated. In addition, the flexural strength of annealed parts is measured via three-point bending tests. Next, it was endeavored to transform the intensity profile of a TEM_{00} CO_2 laser beam with a field-mapping beam shaper, the primary goal being to obtain a beam transformation which created a more uniform intensity distribution. Beam profile measurements were conducted in two regimes (focal plane and far-focal range) in an attempt to identify various profile transformations that correspond to theoretical models. Finally, a fiber-fed laser-heated process was developed for the additive manufacturing (AM) of glass parts. Soda-lime and stripped quartz SMF-28 optical fibers with diameters ranging from 100-125 μm were fed into a laser generated melt pool. A CO_2 laser beam is focused onto the intersection of the fiber and the work piece, which is positioned on a four-axis computer controlled stage. Through the careful control of process parameters such as laser power, feed rate and scan speed, bubble free parts such as walls and lenses may be printed, as well as complicated free-standing structures.

ACKNOWLEDGEMENTS

I would first like to thank Dr. Ed Kinzel for your guidance and mentorship. It is doubtful whether or not I would have pursued a higher education without your influence in my academic career. Thank you also to Dr. Doug Bristow and Dr. Robert Landers, for your encouraging words and enthusiasm for our work, which was truly contagious. In addition, thank you to Dr. Jonathon Goldstein and the Air Force Research Laboratory, your expert advice and funding made this degree possible.

To my beautiful wife, Madison. Your love and support over the past several years has been the lifeblood that I needed to keep going. From the first day that we met you have inspired me to become a better man, and now I know that there is nothing I can't accomplish with you by my side. I can't wait to see what adventures life has in store for us.

Last but not least, my Mom and Dad. Words are futile when it comes to describing how indebted I am to you, it feels cheap to even try to put my thankfulness into words. Whatever success I go on to achieve in life is due to you, I only hope to make you half as proud as I am to say that I am your son.

TABLE OF CONTENTS

Page

ABSTRACT iii

ACKNOWLEDGEMENTS iv

LIST OF ILLUSTRATIONS vii

LIST OF TABLES xii

SECTION

1. INTRODUCTION 1

1.1. SELECTIVE LASER SINTERING 1

1.2. FIBER-FED ADDITIVE MANUFACTURING OF GLASS 3

2. SELECTIVE LASER SINTERING OF SILICA PARTS 6

2.1. SLS EXPERIMENTAL PLATFORM 6

2.2. DIMENSIONAL ACCURACY 8

2.3. DENSIFICATION 10

2.4. FLEXURAL STRENGTH TESTING 14

2.5. SILICA SLS CONCLUSIONS 16

3. OPTICAL BEAM SHAPING 19

3.1. BEAM SHAPING THEORY 19

3.2. BEAM SHAPING EXPERIMENTAL PLATFORM 21

3.3. BEAM SHAPING RESULTS 22

4. FIBER-FED LASER-HEATED ADDITIVE MANUFACTURING OF GLASS 32

4.1. LASER-HEATED EXPERIMENTAL SETUP 32
4.2. FIBER FEEDER DESIGN 33
4.2.1. Hyperdermic Assembly. 34
4.2.2. Feeder Body 37
4.3. SODA-LIME FIBER DEPOSITION 38
4.3.1. Track Morphology. 39
4.3.2. Transmissivity Measurements. 40
4.3.3. Lens Deposition. 41
4.3.4. Two-Dimensional Patterns.....43
4.3.5. Three-Dimensional Parts. 46
4.4. QUARTZ FIBER DEPOSITION 47
4.4.1. Single Track Morphology. 47
4.4.2. Monolayers. 48
4.4.3. Transmissivity Measurements. 49
4.4.4. Quartz Lens Deposition. 55
4.4.5. Three-Dimensional Parts 60
BIBLIOGRAPHY 63
VITA 66

LIST OF ILLUSTRATIONS

Figure Page

2.1. Experimental SLS Platform (top) Powder Bed AM Technique Diagram (bottom) 7

2.2. Dimensional Excess Associated with Different Ratios of Laser Power to Scan Speed 9

2.3. Powder Bed Showing Recessed Sintered Regions 10

2.4. Densification Band in The Powder Bed..... 11

2.5. Effect of Laser Power on Densification Band Thickness 12

2.6. SEM Images of Sintered Silica Post-Deposition (left) And Post-Annealing at 1400 °C (right)..... 13

2.7. Densification Resulting from Annealing Silica Samples..... 13

2.8. Flexural Strength of Silica Samples Annealed at Various Temperatures..... 15

2.9. Fractured Silica Beams Post Three-Point Bending Test..... 15

2.10. Characteristic Load vs. Deflection Experimental Data for Fractured Silica Samples..... 16

2.11. Flexural Strength of Silica Deposited at Varying Scan Speeds..... 16

2.12. Structures Created via SLS Platform (As-Printed) 17

3.1. Illustration of Energy Lost for Expansion Beam Shaping [22] 19

3.2. Ray Diagram of Uniform Intensity Beam Shaping Optical Element [24]..... 20

3.3. Beam Size Before Expansion (left) After Expansion (right) 21

3.4. Experimental Setup (top) Schematic of Beam Shaping Optical System (bottom) 21

3.5. Theoretical Intensity Profiles Near Focal Plane [29]..... 22

3.6. Matched Experimental Intensity Profiles Near Focal Plane 23

3.7. Possible Shaped Intensity Profiles: Waist (left), And Flattop (right) 24

3.8. Intensity Profiles Measured Away from The Focal Plane (left) Compared to Theoretical [29] Counterparts (right) 25

3.9. Additional Profiles Observed Which Were Not Predicted with Theoretical Model 25

3.10. Beam Location Before Shaping (top), After Shaping (bottom) 26

3.11. Theoretical Model of Intensity Distribution in Beam with Misaligned Beam (top), Experimental Profile of Misaligned Beam (bottom) 27

3.12. Comparison of Unshaped Beam (left), Shaped Beam (right) 28

3.13. Scorch Marks on Photoreactive Beam of Shaped Beam (left), Unshaped Beam (right) 29

3.14. Single Track Scans of 1 mm Diameter Soda-Lime Filaments with Gaussian Beam (left), Shaped Beam (right) 29

3.15. Single Track Scans of 2mm Diameter Soda-Lime Filaments with Gaussian Beam (left), Shaped Beam (right) 30

3.16. Borosilicate Track Scanned with Gaussian Beam (left), Quasi-Uniform Intensity Beam (right) 30

4.1. Schematic of Experimental Platform 32

4.2. Process Parameters for Fiber-Printing Specified for Their Effect on the Deposited Glass 33

4.3. Schematic of Telescoping Hypodermic Tubing Used to Prohibit Fiber Deflection .. 35

4.4. Fully Assembled Hyperdermic Assembly 36

4.5. Fiber Feeder Body Design 38

4.6. Fiber Feeder with Span, d, Identified as Critical Parameter to Prevent Fiber Buckling 38

4.7. Cross Section of Single Tracks with Measured Dimensions Labeled 39

4.8. Recorded Dimensions of Single Track Morphology as s Function of ProcessParameters 40

4.9. 2D Wall Post-Deposition (left), After Polishing to Create Transmissivity Sample (right) 40

4.10. Schematic of Transmissivity Measurement Setup 40

4.11. Measured Extinction Coefficient of Deposited Fiber Versus Laser Power 41

4.12. Simple Lens Printed with Soda-Lime Fiber Post-Deposition: Top View (left), Side View (right) 42

4.13. Printed Lens Post-Deposition Demonstrating Ability to Focus Light 42

4.14. Path Generated to Deposit S&T Cog (left) Deposited Soda-Lime S&T Cog Pattern (right) 43

4.15. S&T Logo Outlined with Fiber (top left) Filled S&T Logo Prior to Reflowing (bottom) S&T Logo Fluorescing Under a Blacklight Post Reflowing (top right) ... 44

4.16. Deposition Path Generated for 'Joe Miner' Profile (left), Pattern Post-Deposition (middle), Pattern Fluorescing Under $\lambda = 405$ nm Light (right) 44

4.17. Artwork Desired to be Deposited (top left), Path Generated for Deposition (top right), Pattern Post-Deposition (bottom left), Pattern Fluorescing Under $\lambda = 405$ nm Light (bottom right) 45

4.18. Free-Standing Spiral Deposited with Fiber-Fed Process 46

4.19. A-Frame Truss Walls Deposited Entirely with Eu2O3 Fiber (top) A-Frame Truss Walls Deposited with Soda-Lime Fiber Both Doped and Un-Doped with Eu2O3 (bottom) 47

4.20. Regimes of Single Track Fiber Deposition 48

4.21. Monolayers Deposited with Various Track Spacings 49

4.22. Walls Deposited with Quartz Fiber for Transmissivity Measurement 50

4.23. Transmissivity of Quartz Walls Deposited at Various Laser Powers 51

4.24. Melt Pool Temperature Data Collected During Monolayer Deposition for Various Laser Powers (left), Average Melt Pool Temperature Versus Laser Power (right) 52

4.25. Radiation Spectra of Quartz Fiber Melt Pools Around Vaporization Threshold 53

4.26. Inclusion-Free Block of Quartz Glass (3×1×1 mm) Deposited with Fiber-Fed Approach 54

4.27. HeNe Laser Beam Incident on Wall After Transmission Through: (a) Air, (b) Printed Quartz Block, (c) Quartz Wall Printed at P = 10.8 W, and (d) Quartz Wall Printed at P = 6.6 W 55

4.28. (a) Monolayer Patterns Used to Create Cylindrical Profile, (b) Polished Cross-Section of Deposited Cylindrical Lens, (c) Cylindrical Lens Imaging 1951 AFRL Resolution Test Chart, (d) Bare HeNe Laser Beam, (e) HeNe Beam Transmitted Through Cylindrical lens 56

4.29. Oblique View (left) and Top-Down View (right) of Simple 3D Printed Quartz Lens 57

4.30. Simple Lens Optically Focusing Light (left) Imaging AFRL Resolution Test Chart (right) 57

4.31. Cross-Section of Lens Profile Design (top) Progression of Lens Deposition (bottom) 58

4.32. Profile of Spherical Lens (top left), Lens Imaging Pixels on LCD Monitor (bottom left), AFRL Resolution Test Chart with No Lens (top right), AFRL Resolution Test Chart Imaged Through Spherical Lens (bottom right) 59

4.33. Simple Geometries Deposited with Quartz SMF 60

4.34. St. Louis Gateway Arch Generated Deposition Path (left) Structure Post-Deposition (right) 61

4.35. Fiber Truss in Various Stages of Deposition 62

LIST OF TABLES

Table Page

4.1. Gauges and Dimensions of Hyperdermic Tubes in Hyperdermic Assembly……..35

1. INTRODUCTION

Additive manufacturing has revolutionized the field of manufacturing in recent years due to the advantages that these processes entail. Traditionally these advantages have pertained to an increased design freedom and the allowance of complicated three-dimensional geometries, rapid prototyping, more efficient material usage, and the capability to manufacture parts from functionally graded materials. As these techniques for additive manufacturing mature however, more manufacturing applications become candidates for adaption to these processes. Specifically, applications for optical systems are emerging as a promising enterprise; applications such as photonics packaging, gradient index (GRIN) and freeform optics, and integrated optics all stand to benefit from the development of a system which is capable of depositing high quality optical materials. This is due in part to the attractive material properties of glass itself. Glass is transparent in the visible spectrum, is amorphous and therefore does not suffer from grain boundary scattering, it is chemically inert, harder than transparent polymer counterparts, and displays a low sensitivity to temperature gradients.

1.1. SELECTIVE LASER SINTERING

Selective Laser Sintering (SLS) is a powder-based additive manufacturing process which utilizes a laser to locally heat powdered material, thus fusing particles in accordance with a two-dimensional pattern created within a modeling program. The deposition of consecutive powder layers then allows for the fabrication of complex three-dimensional parts, which are in turn supported by previously sintered layers and the surrounding powder itself [1]. While the SLS of metals and polymers has been

investigated and documented extensively [2][3], the adaption of SLS platforms for the fabrication of ceramic structures has received very little attention, due in part to complications resulting from the process's fast cooling cycles [1]. Additionally, the SLS of brittle materials often results in the formation of cracks in the part during the building process, and any ceramic parts which are successfully fabricated exhibit mechanical strengths much lower than those of conventional ceramics [4].

The SLS process traditionally operates through the atomic diffusion and binding of the structural powder at temperatures well below its melting point [5]. However, a solid binder may be utilized to aid in the manufacturing of ceramic parts, where the binder is mixed with the ceramic powder and is subsequently melted by the laser, thus enveloping the ceramic powder via capillary forces. However, this method does not melt the ceramic powder itself, and therefore requires an additional step wherein the fabricated part is heated in a furnace to impart strength to the structure; or depending on the application, remove the binder from the part all together [1]. However, another category of SLS has potential for fabricating 3D geometries without using a binding material. Solid State Sintering (SSS) is a thermal process which occurs at temperatures ranging from $T_{melt}/2$ and T_{melt}, where T_{melt} is the melting temperature of the material. Therefore SSS encourages atomic diffusion within the powder, meaning that this process is applicable for a wide range of materials provided the platform is capable of reaching the required temperature [6].

Additionally, conventional SLS platforms rely on rollers or wipers to deposit additional powder layers, allowing for the rapid manufacturing of functional parts. However, these distribution techniques are negatively impacted by the particle geometry

of the powder being spread, and the roller/wiper often damages the fragile structure sintered in the previous powder layer. In addition, the quality of parts fabricated with SLS increases when the grain size of the powdered material decreases. However, the frequency of agglomerations on the sintered surface increases with a decreasing grain size, making further powder layer depositions impossible with a conventional wiper or blade [7]. Attention has been given to improving the conventional powder spreading process by studying the impact of the wiper/roller motions on the density and homogeneity of the resulting powder layer, but at present the most effective means of achieving a more homogeneous powder layer is to compress the powder as it is being spread [8], which only serves to further increase the direct shear loading on the sintered structure below.

This study aims to fabricate functional silica gel parts via SLS/SSS (with no binding agent), and in doing so investigate alternative powder distribution techniques which operate in a manner to enable the rapid manufacturing of three-dimensional parts, and which also offer advantages over the conventional wiper/roller approach. Once parts are successfully fabricated, they will then be characterized to identify the SLS platform parameters that result in the highest dimensional accuracy and structural integrity of the fabricated parts. Moreover, annealing parts after deposition is investigated as a means for increasing mechanical strength.

1.2. FIBER-FED ADDITIVE MANUFACTURING OF GLASS

While additive manufacturing has been widely studied for use with polymers, metals and ceramics, there is comparatively little work done in developing AM

techniques for glass [9]. Those studies which have been conducted into the AM of glass share a limitation in depositing transparent glass due to bubble entrapment. Several groups utilizing selective laser sintering were able to fabricate three-dimensional glass parts [10][11][12], but these parts resemble sugar cubes in both texture and appearance. The development of continuous melting approaches for glass AM by several groups has been much more successful in depositing transparent glass. A filament-fed laser-heated process developed by Luo et al. demonstrated an ability to deposit void-free transparent glass using a feedstock with diameters ranging from 0.5-3 mm [13]. However, this process requires new cane to be reloaded into the filament feeder intermittently during the deposition process, and even the smallest diameter feedstock used of 0.5 mm cannot be rolled to extend the duration of uninterrupted deposition. Klein et al. developed a gravity-fed molten vat approach [14], after which Micron3dp introduced their high temperature extrusion technique [15]. Both of these platforms are capable of depositing very intricate three-dimensional geometries out of glass, but the inability of these techniques to deposit void-free blocks of glass constrains their use for optical applications.

In light of the limitations with the filament-fed laser-heated process [13], a system utilizing optical fiber as a feedstock is very attractive, as kilometers of fiber may be spooled to allow for a continuous deposition process. In addition, the smaller diameter of optical fiber minimizes issues with thermal diffusion in the feedstock, potentially allowing for a greater volumetric deposition rate than that of the filament-fed process. Optical fibers are widely available, consisting of extremely high quality, low loss glass (<1 dB/km), and are relatively cheap with prices lower than $180 per km of single mode

fiber [16]. However, there are certain challenges involved with using fiber feed-stock. For instance, most commercially available fibers include an acrylic coating designed to prevent the fiber from fracturing along microcracks. This coating must be removed in order to achieve the highest transmissivity in deposited parts. Also, the small diameter of the fiber means that it is easier to deflect and buckle during the feeding process. These issues must be overcome in creating a fiber-fed additive manufacturing process.

2. SELECTIVE LASER SINTERING OF SILICA PARTS

2.1. SLS EXPERIMENTAL PLATFORM

The SLS platform used in these experiments is based on a repurposed laser cutting system equipped with a 40 W CO_2 laser (see Figure. 2.1). A three-mirror assembly directs the laser, with the last mirror fixed to a carriage that is positioned on a translational rail that deflects the beam downwards by ninety degrees, through a lens onto the powder bed (Figure 2.1). The SLS process takes place in a room temperature laboratory environment and the laser has a spot measured size of 254 μm at the substrate. The parameters varied to affect the quality of the sintered structure were the laser power [W] and scan speed [mm/s].

Small granular particles are preferred for the powder as these powders require less energy [17] to melt and improve the surface quality of the sintered surface. Therefore, silica gel (Silica Prep TLC Premium RF) was selected with these considerations in mind and also for its low coefficient of thermal expansion (CTE) of approximately 10^{-6}/°C. The silica gel has a particle size of 15-40 μm, a bulk density of 0.5 g/cm^3, and a porosity of 60 Å. The silica powder was then deposited onto a 75×25 mm quartz slide which acted as a substrate. The silica powder was distributed via a sifter technique, which utilizes a silica-filled container with a fine mesh on the bottom. The vessel is then vibrated, which results in the powder being sifted out onto the substrate below; resulting powder layers are distributed with a thickness of 0.65 ± 0.15 mm. While conventional SLS platforms deposit powder layers by spreading the powder across the build area with a wiper; and frequently damaging the fragile sintered structure below, the sifter distribution technique benefits from the ability to quickly deposit additional layers of powder without subjecting

the sintered structure to shear loading during the deposition process. Additionally, while the conventional method of spreading powder with a wiper is sensitive to the geometry of the silica particles [1], the shaker technique was found to be equally capable of distributing granular particles as it is spherical particles.

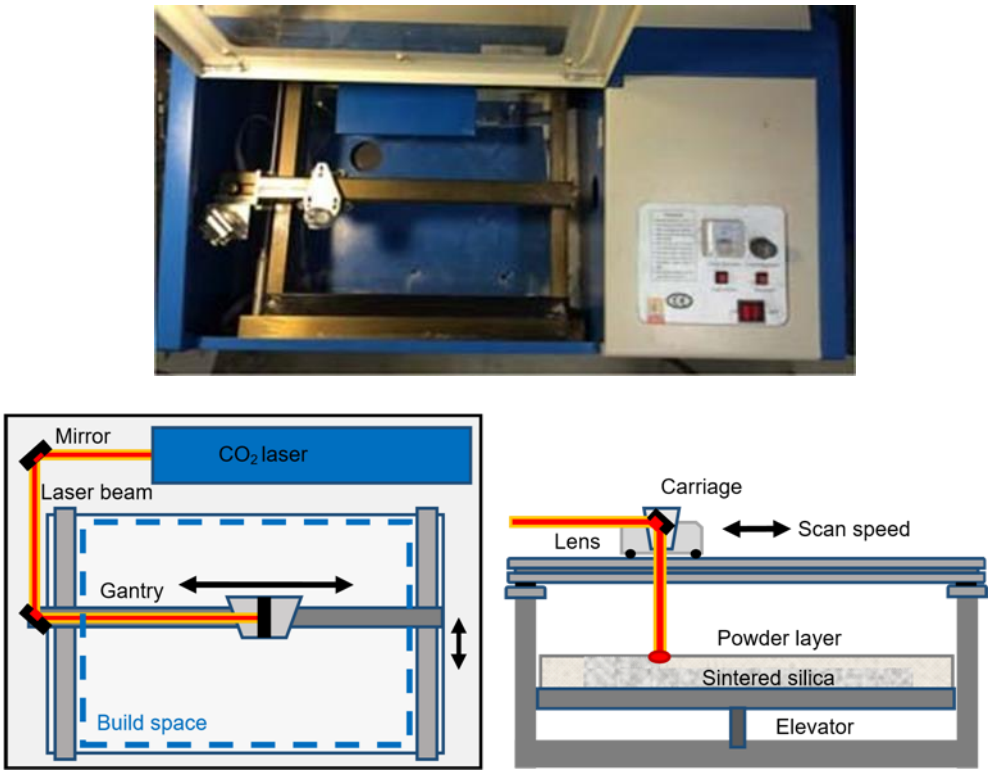

Figure 2.1. Experimental SLS Platform (top) Powder Bed AM Technique Diagram (bottom)

Perhaps the most critical powder bed characteristic associated with strong, cohesive structures is the consistency in thickness of the distributed powder layers. By decreasing the powder layer thickness as much as possible, consecutive sintered layers are more likely to solidify as a single structure. If the powder layer thickness varies from one deposition to the next, so too will the cohesive strength of the sintered layers. In

some cases, if a single powder layer is too thick, structural unification is lost and the final part separates along that particular layer. Additionally, a reduction in the powder layer thickness allows for a higher scan speed, as the depth of sintering required to fuse particles to the previous layer is reduced [17]. However, too thin of a powder layer risks a stepping effect [18], wherein the sintering depth exceeds the powder layer and decreases dimensional accuracy. Therefore, a decreasing powder layer depth must correspond to a decrease in laser power or an increase in scan speed. A study by Bertrand et al. stipulates that the powder layer thickness should be ten times greater the average particle diameters [8].

2.2. DIMENSIONAL ACCURACY

To precisely design the shape of SLS parts, it is important to determine the appropriate laser power and scanning speed. In particular, these parameters change the sintered area of the powder due to different temperature distributions. This affects the final geometry of the part and can lead to deviations from the desired shape. The effect of different combinations of laser power and scan speed on the accuracy of the resulting specimen geometry was investigated. Single layer square patterns with a 0.75 mm height and different specified widths, w_0, of 5, 10, and 15 mm were deposited using the system. The width of the deposited structures, w, was measured for different combinations of laser power and scan speed. The results showed that for the same ratio of laser power to scan speed, a consistent amount of powder is fused along the boundary of the desired sintered region, regardless of the size of the pattern, which was also observed in previous studies [19]. Therefore, the width of the sintered region can be modeled using the

expression $w=w_0+\delta$, were δ is the error in the width dimension and is a function of laser power and scan speed.

The error in the dimensions of 10×10 mm^2 square patterns with a 0.75 mm height was determined for several combinations of laser power and scan speed. The scan speed was varied from 100 mm/s to 300 mm/s in 50 mm/s increments while maintaining one of several iterations of specified laser power. The dimensions of the sintered regions were measured with electronic calipers, and the values of δ were determined for different ratios of laser power to scan speed (Figure 2.2).

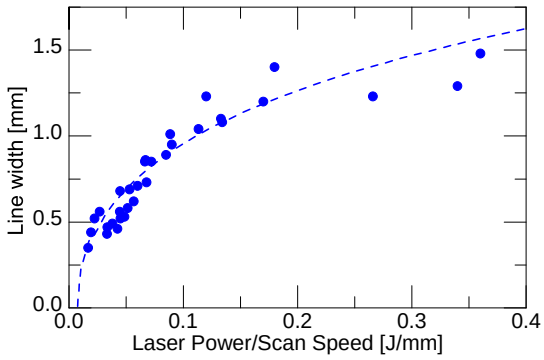

Figure 2.2. Dimensional Excess Associated with Different Ratios of Laser Power to Scan Speed

The trend of the line width versus the ratio of laser power to scan speed shown in Figure 2.2 supports the theory that the dimensional excess of sintered parts is a result of energy flux from the laser spot to surrounding particles. This energy flux causes particles adjacent to the laser spot to melt. Increasing the power supplied to the laser increases the energy flux density and a larger area of particles surrounding the laser beam is melted. This conclusion is corroborated by Klocke et al., who found that increasing the laser

power leads to an increase in the density of the specimen, as well as creating a larger melt pool [17].

2.3. DENSIFICATION

A phenomenon observed to be present in every test of the SLS platform is that when a region of powder is sintered, there is a subsequent height difference between the sintered surface and the surrounding powder bed, as shown in Figure 2.3. These regions are consistently recessed within the powder bed by 0.12 ± 0.06 mm when sintered with a laser power of 19.5 W and a 200 mm/s scan speed.

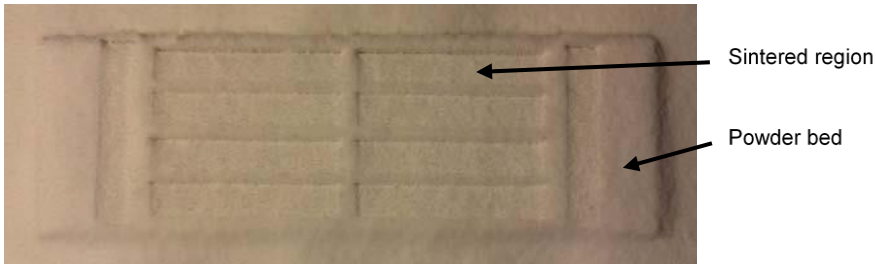

Figure 2.3. Powder Bed Showing Recessed Sintered Regions

The depressed nature of the sintered pattern complicates the construction of three-dimensional shapes that include variations in its cross-sectional area along the height of the structure; if a sintered pattern includes an area of previously un-sintered powder bed, the desired outcropping will be formed at a greater height than previously sintered regions connected to it. This results in a wavy surface.

The density of the sintered silica is 0.41 g/cm^3 on average. This constitutes a decrease in density of approximately 18% from the theoretical density. If the height

difference between sintered regions and the surrounding powder bed was the result of densification occurring during the sintering process, Eq. (1) would predict the height ratio of the sintered region to the powder bed by assuming that the mass, length, and width of the region remain constant. Eq. (1) dictates however that if the height of the sintered region decreases, then it is required that the density of the sintered silica increases. By weighing the powder bed before and after a region is sintered, it has been determined that there is a mass loss of 0.0146 ± 0.0032 g when sintering using a laser power of 19.5 W and a scan speed of 200 mm/s. By taking this mass loss into account, it is possible that the recessed height of sintered regions is the result of densification occurring during the sintering process. Explaining this loss of mass is still subject to ongoing research.

$$\frac{h_{sinter}}{h_{powder}} = \frac{\rho_{powder}}{\rho_{sinter}} \quad (1)$$

Figure 2.4. Densification Band in The Powder Bed

It has also been observed that when the laser begins to sinter a region of unfused powder, there is a significant amount of densification occurring along the pattern where the laser first traverses (see Figure 2.4). These depressed regions are almost entirely

confined to a thin layer of the fused pattern in the negative-y direction, as these are the regions in which the laser first begins to sinter the powder bed.

The laser power was decreased to determine if thickness of the densified bands could be reduced. In the interest of preserving the mechanical strength of the sintered silica, the laser power-to-scan speed ratio corresponding to a qualitatively optimal sintered silica part (19.5/200 [J/mm]) was preserved as the power was decreased. The thickness of the densification band present for each of the laser powers tested were then measured and are shown in Figure 2.5.

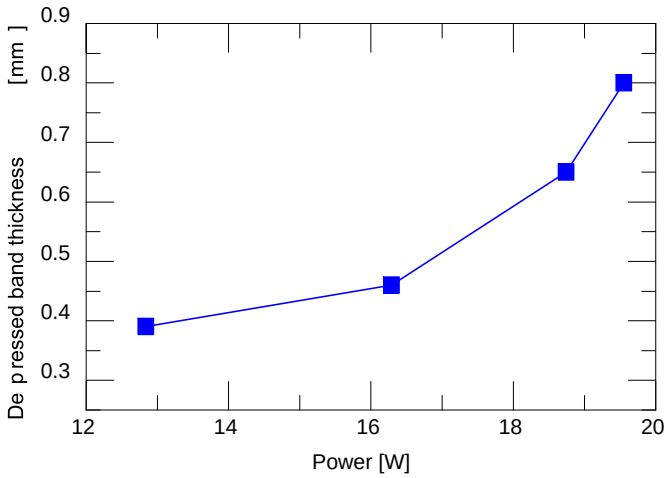

Figure 2.5. Effect of Laser Power on Densification Band Thickness

Due to the porosity of parts fabricated using SLS, their mechanical strength is reduced. In order to increase strength by increasing density, SLS parts were annealed at various temperatures. Several sintered silica bar samples were weighed and their dimensions recorded before they were annealed in an oven at a specified temperature for a soak time of thirty minutes. After being slowly cooled down to room temperature at a

rate of 1°C per minute to avoid incurring destructive thermal stresses, the dimensions of the bars were again measured and the parts weighed. SEM images taken of silica samples post-fabrication and post-annealing reveal that the annealing process does little to decrease the porosity of the parts (Figure 2.6). The estimated densification resulting from annealing the silica samples at temperatures ranging from 1000-1400°C is depicted in Figure 2.7. A maximum density of 0.66 g/cm^3 results from annealing the silica at 1250°C, after which the density plateaus for higher annealing temperatures.

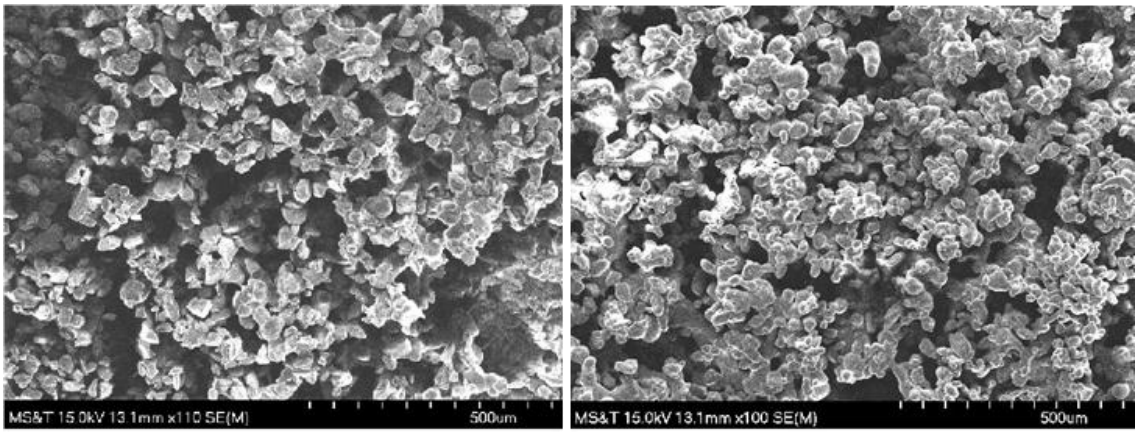

Figure 2.6. SEM Images of Sintered Silica Post-Deposition (left) And Post-Annealing at 1400 °C (right)

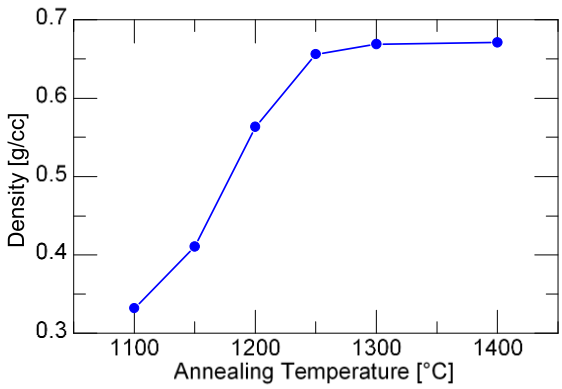

Figure 2.7. Densification Resulting from Annealing Silica Samples

2.4. FLEXURAL STRENGTH TESTING

The flexural strength of sintered and annealed silica beams with rectangular cross-sections of 4×3×20 mm^3, were measured in accordance with ASTM standards [20]. In determining the flexural strength of the ceramic specimens produced via SLS, a three-point bending test was utilized with a fully-articulating fixture. The flexural strength of the specimens were determined via Eq. (2) [20]

$$S = \frac{3PL}{2bd^2} \tag{2}$$

where P is the maximum load present at failure, L is the unsupported span of the test specimen, b is the specimen width, and d is the specimen thickness. Failure was identified by a 50% decrease in applied load corresponding to a near-constant value of deflection. Note that the dimensions used in Eq. (2) are those measured post-annealing, and not the nominal dimensions.

The flexural strength of silica samples annealed over a range of temperatures is plotted in Figure 2.8. An annealing temperature of 1250°C results in a maximum mean flexural strength of 3.165 MPa for a sample size of ten beams. However, the flexural strength then decreased to approximately 50% of this maximum value when annealing at temperatures greater than 1250°C. Whether or not this drop in strength is due to a crystallization which takes place which is subsequently degraded at higher temperatures, or some other effect of the material behavior, is unknown at this time. However, it is possible that the soak time of thirty minutes when annealing is not sufficient for

imparting a maximum amount of strength to the samples, which may also explain why the densification of the silica plateaus around this same anneal temperature of 1250°C.

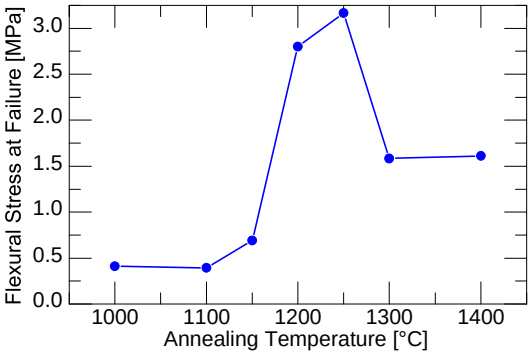

Figure 2.8. Flexural Strength of Silica Samples Annealed at Various Temperatures

Figure 2.9. Fractured Silica Beams Post Three-Point Bending Test

The fracture surfaces of specimens after failure (shown in Figure 2.9) exhibit jagged cracks. The cracks propagated from one powder layer to the next, resulting in localized peaks in the load vs. deflection plot that correspond to individual powder layer fractures (see Figure 2.10). The crack propagation through a fracturing specimen may be altered to more closely resemble traditional behaviors of conventional linear elastic, homogeneous materials by decreasing the powder layer thickness, which improves the likelihood of a cohesive bond with the substrate below. However, decreasing the powder layer thickness necessitates that more layers be deposited overall to produce a part with the same height, which decreases the productivity of the platform.

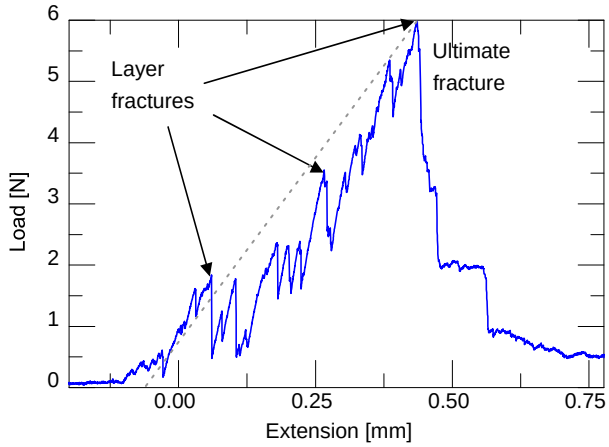

Figure 2.10. Characteristic Load vs. Deflection Experimental Data for Fractured Silica Samples

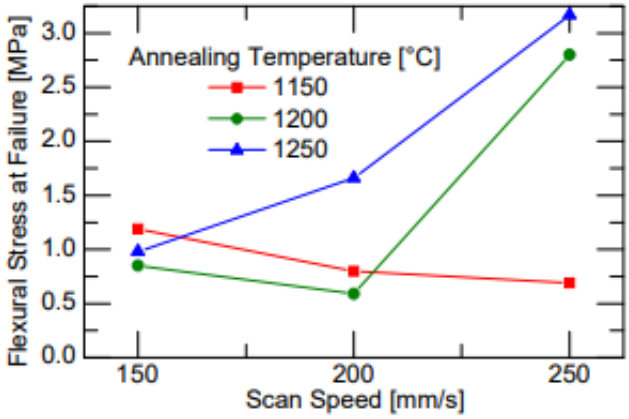

Figure 2.11. Flexural Strength of Silica Deposited at Varying Scan Speeds

2.5. SILICA SLS CONCLUSIONS

The SLS platform developed was used to manufacture complex three-dimensional geometries, some of which may also involve the fusion of previously un-connected structures (see Figure 2.12). The parameters identified as producing optimal sintered structures are a laser power of 19.5 W and a scan speed of 200 mm/s. The density of the sintered silica associated with these parameters was found to be 0.4146 g/cm^3, following a mass loss of 0.0146±0.0032g during the sintering process. The density was further

increased to 0.67 g/cm^3 by annealing the sintered silica at a temperature of 1250 °C for a soak time of thirty minutes. In addition to densifying the silica, the annealing process also resulted in increased flexural strength. In particular, a maximum flexural strength of 3.165 MPa was observed for parts annealed at 1250°C.

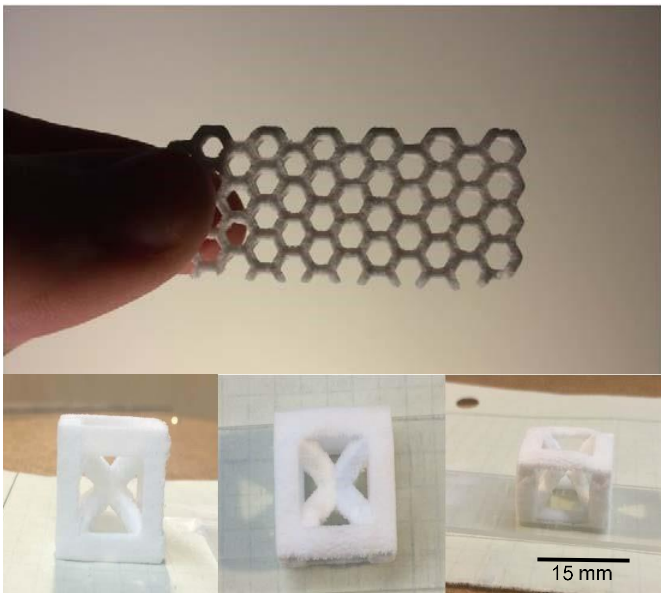

Figure 2.12. Structures Created via SLS Platform (As-Printed)

The sifter powder distribution method needs to be refined before further investigations into the fabrication of silica with SLS may be conducted. The large powder layer depth and variations in layer thickness limit the part's geometrical precision. This also results in variations in the mechanical strength of silica parts which is likely to impact the observed trends. Work should be done to improve powder distribution by attaching the sifter to the carriage on the gantry in the SLS platform to allow a consistent amount of powder to be deposited for each layer, as well as to increase the control over the depth of the deposited powder layer.

The high porosity of the parts complicated the traditional Archimedean method for determining a part's volume [21], which necessitated a volume approximation via electronic calipers instead. A more accurate means for determining the volume of deposited silica parts would result in more accurate calculations of flexural strength. Also, it should be investigated whether or not further densification occurs for annealing temperatures greater than 1250°C and for soak times greater than thirty minutes, as further densification may also correlate to an increase in flexural strength.

3. OPTICAL BEAM SHAPING

3.1. BEAM SHAPING THEORY

There are many applications which would benefit from a variation in the intensity profile of a laser beam to provide a uniform temperature profile on a workpiece, such as scribing, PCB drilling, holography, lithography, welding, and many more. However, typical laser beams used in laser assisted processes have an intensity distribution which are described by a Gaussian function, which has a very high energy concentration along the axis of the beam. One solution for achieving a uniform intensity distribution with a TEM_{00} beam is to greatly expand the beam to create a quasi-uniform intensity distribution from the tip of the intensity profile, and simply discard of the larger intensity gradient along the 'wings' of the beam. This is an unattractive solution however, as typically up to 50% of the beam energy is lost (Figure 3.1).

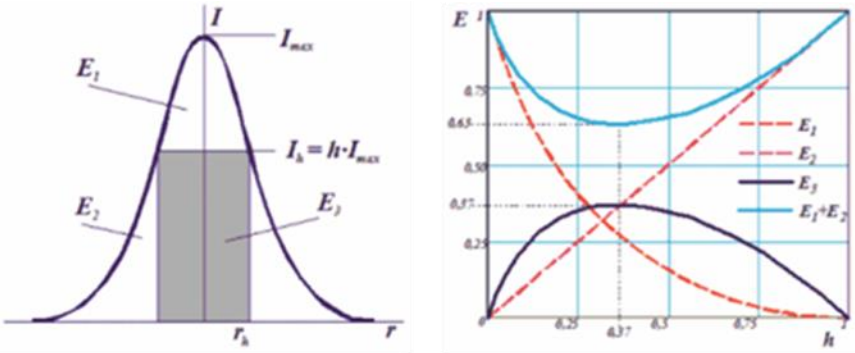

Figure 3.1. Illustration of Energy Lost for Expansion Beam Shaping [22]

In comparison, refractive beam shapers of the field-mapping type are a more appealing means for producing uniform intensity profiles. The operating principle of a

beam shaper is not to discard excess energy from the Gaussian profile, but to instead transform the intensity distribution of the laser beam to achieve a desired profile, while conserving a majority of the beam's energy in the process. Such devices are commonly implemented as telescopic systems with two optical components: The accurate inducing of a wave aberration in the first optical component, and the compensation for this aberration in the second optical component [23]. These optical components are designed to provide an equal path length for all transformed rays to ensure that the wave front is flat at the output, thus creating a uniform intensity beam with very low divergence [24]. While it is possible to construct a field-mapping beam shaper with spherical lenses, each optical element will necessarily consist of several spherical lenses, which is very difficult to design. The reshaping of a laser beam using only a pair of aspheric lenses (Figure 3.2) was first proposed by Frieden [25] and Kreuzer [26], and later by Shealy and co-workers [27]. Essentially an anamorphic variant of a Galilean beam-expanding telescope with radially varying magnification, this arrangement provides better performance in a more compact design [28]. A ray diagram of an aspheric beam shaper may be seen in figure 3.2.

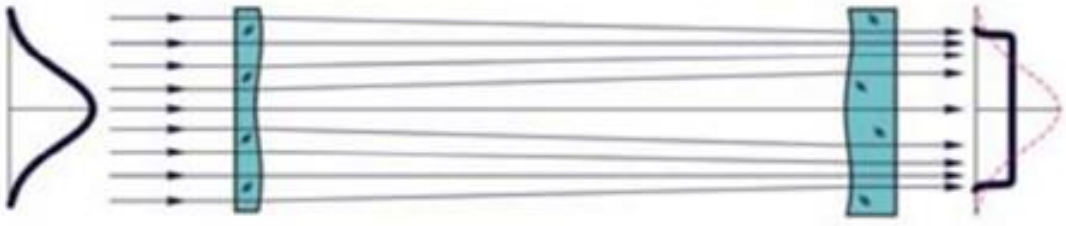

Figure 3.2. Ray Diagram of Uniform Intensity Beam Shaping Optical Element [24]

3.2. BEAM SHAPING EXPERIMENTAL PLATFORM

The beam shaper used for generating intensity profile transformations was a Focal-πShaper 12_CO2_10.6 manufactured by AdlOptica. This beam shaper requires an input TEM_{00} beam with a Gaussian intensity distribution with a $1/e^2$ beam width of 8-12 mm. The beam exiting the beam shaper is then collimated with an intensity distribution modeled by an Airy disc. The laser beam to be shaped was generated by a CO_2 Synrad evolution125 with a wavelength of 10.6 μm, which has an unshaped beam diameter of 4.3 mm.

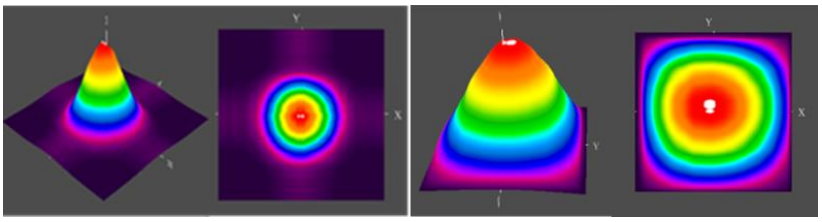

Figure 3.3. Beam Size Before Expansion (left) After Expansion (right)

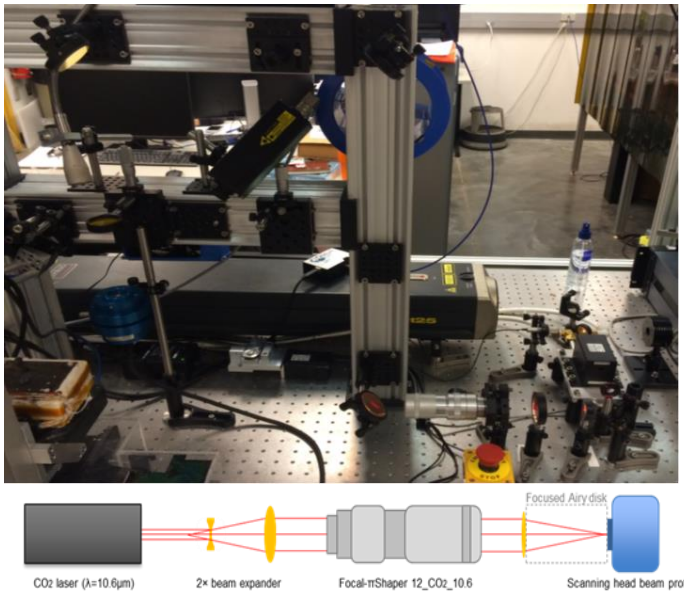

Figure 3.4. Experimental Setup (top) Schematic of Beam Shaping Optical System (bottom)

The beam was first expanded with a Galilean beam expander to a final beam diameter of 8.6 mm (Figure 3.3). After this, the collimated beam passed through the beam shaper and the collimated output beam focused by a lens with a 5-inch focal length and measured with an Ophir Nanoscan scanning-head beam profiler. A diagram of the experimental setup used is provided in figure 3.4.

3.3. BEAM SHAPING RESULTS

One of the claims made about the Focal-πShaper is that the device optimizes conditions of interference near the focal plane to provide a variety of intensity profiles (flattop, donut, inverse-Gauss) [29]. It was therefore desired to characterize the shaped intensity profiles near the focal plane of the focusing lens to not only determine the validity of these claims, but also because these small spot size and high energy concentration profiles are those which are intended for use later in improving material processes. Therefore, profiles were measured within several Rayleigh lengths of the focal plane with the intention of cataloging experimental intensity distributions which correspond to the theoretical intensity profiles depicted in figure 3.5.

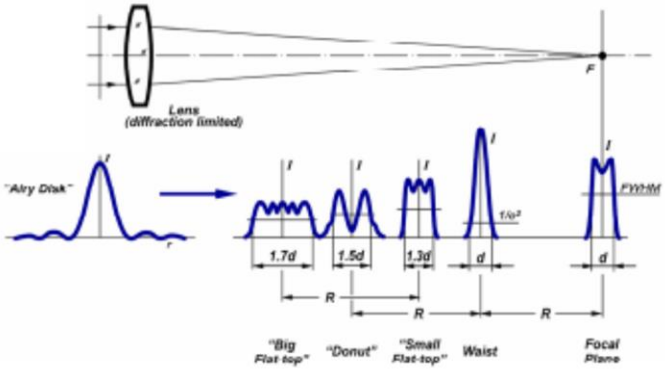

Figure 3.5. Theoretical Intensity Profiles Near Focal Plane [29]

It was found that of the five profiles predicted, only two were able to be replicated experimentally; the focal plane ‘horned’ profile, and the donut (Figure 3.6). The width, d, of the ‘horned’ profile was measured to be 140 µm, while the donut had a measured width of 190 µm, or 1.35d.

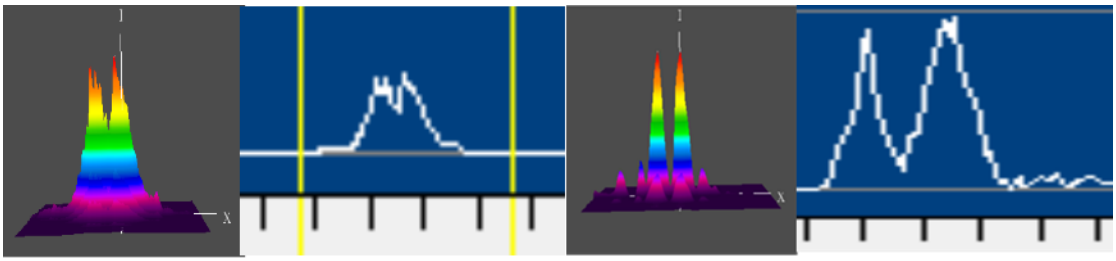

Figure 3.6. Matched Experimental Intensity Profiles Near Focal Plane

Measuring profiles with such small spot sizes proved to be difficult with the beam profiler used. Often the profiles exhibited random peaks and interferences, which would not coalesce into a consistent beam shape. This is likely because the beam profiler software operates by searching for Gaussian profiles, and as a result the measurements may be interpreted with a Gaussian bias. This also complicates profile width measurements, as profiles with relatively steep sides may be artificially extended with Gaussian ‘wings’ which may or may not be present in the shaped beam. There is also a low confidence in the location of these profiles, as it is difficult to manually push the beam profiler with an accuracy of ±50 µm. With these considerations in mind, two additional profiles measured are candidates for shaped beams (Fig 3.7): The flattop (width=2.3d) and waist (width=d).

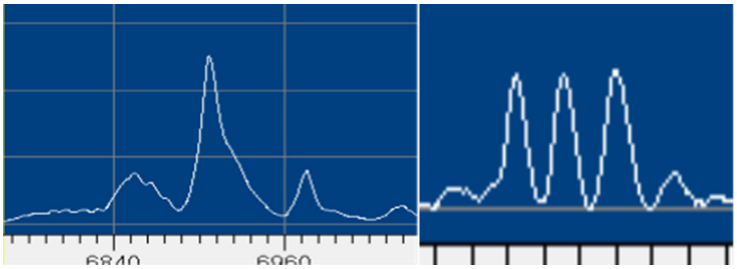

Figure 3.7. Possible Shaped Intensity Profiles: Waist (left), And Flattop (right)

Next, shaped intensity profiles were measured away from the focal plane, where it was hoped that the larger spot sizes may be easier to resolve into identifiable intensity profiles. Once again, it was desired to identify experimental profiles which corresponded to theoretical models. Beam profile measurements taken at 50-90% of the focal length of the focusing lens appear to resemble their theoretical counterparts rather well (Figure 3.8). However, profiles measured between the focal plane and 50% of the focal length diverge greatly from theoretical models. In addition, several profiles measured experimentally take on a shape of their own (Figure 3.9) and bear no resemblance to theoretical profiles found in literature. While these unique profiles may be the result of influence from the beam profiler, the shapes they encompass are still consistent with the evolution of intensity profiles for the rest of the focal range observed, transitioning from one profile matched with theory to the next. Given that one of the easiest ways to change the beam profile with a Focal-πShaper is to change the input beam diameter, it seems likely that these profiles are representative of the true beam shape, and that these profiles diverge from theoretical models because the input beam diameter is 8.6 mm, whereas the theoretical profiles assume an input diameter of 8 mm. To verify this claim, an optical model of the beam shaper would need to be created, and theoretical profiles generated using an input beam more closely related to the beam used in this experiment.

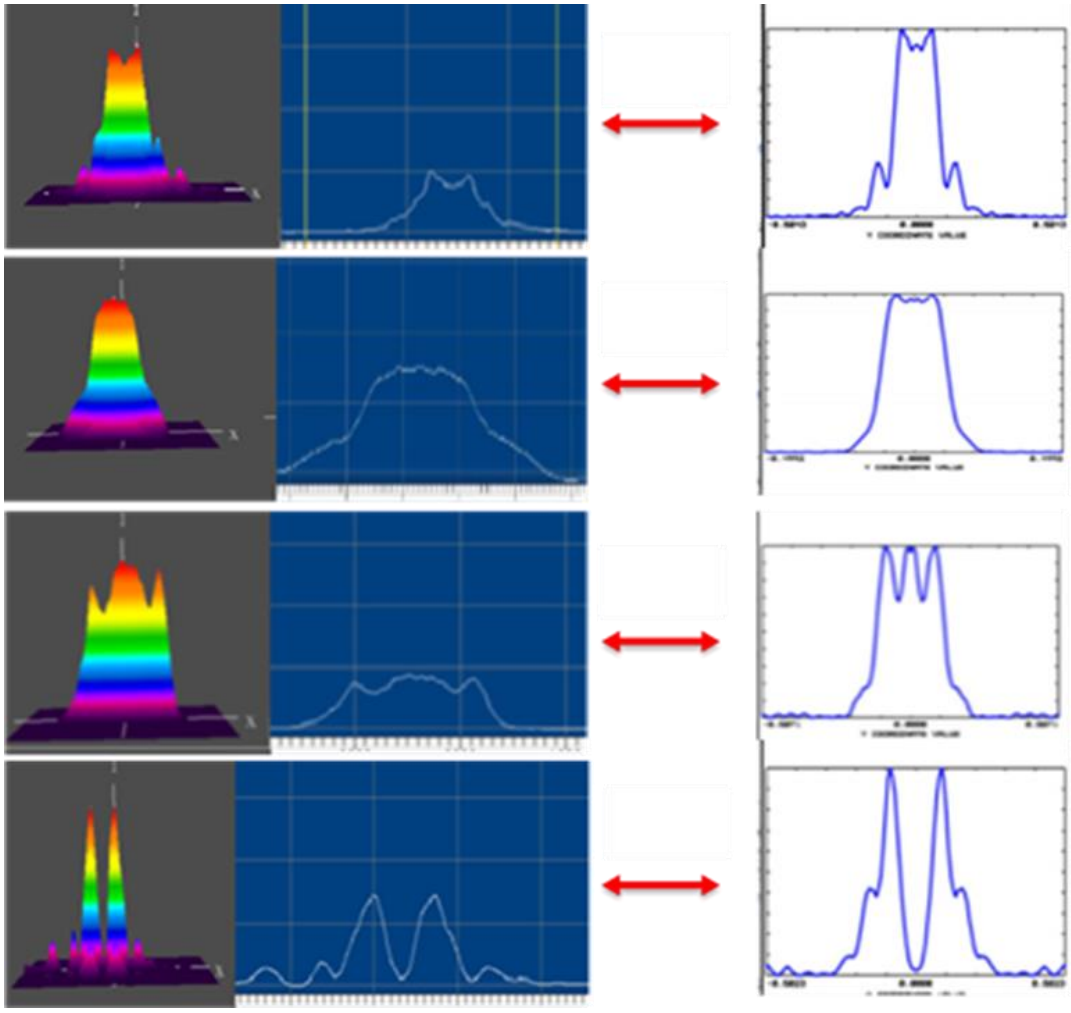

Figure 3.8. Intensity Profiles Measured Away from The Focal Plane (left) Compared to Theoretical [29] Counterparts (right)

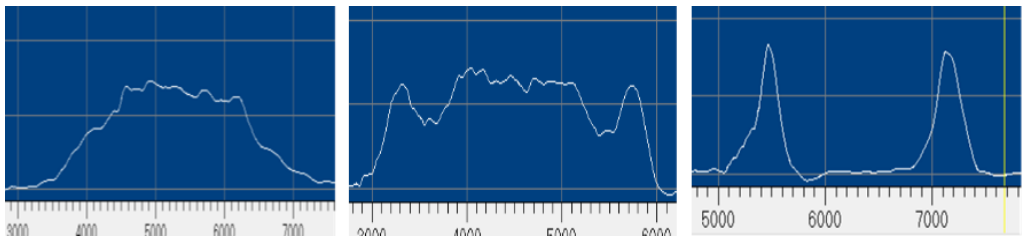

Figure 3.9. Additional Profiles Observed Which Were Not Predicted with Theoretical Model

It was found that the beam exiting the beam shaper was consistently deflected by an angle of 4.6 mrad (Figure 3.10). It was speculated that this deviation angle was the

result of the input beam being misaligned with the optical axis of the beam shaper, but no matter how precisely aligned the input beam and shaper were, the deviation persisted.

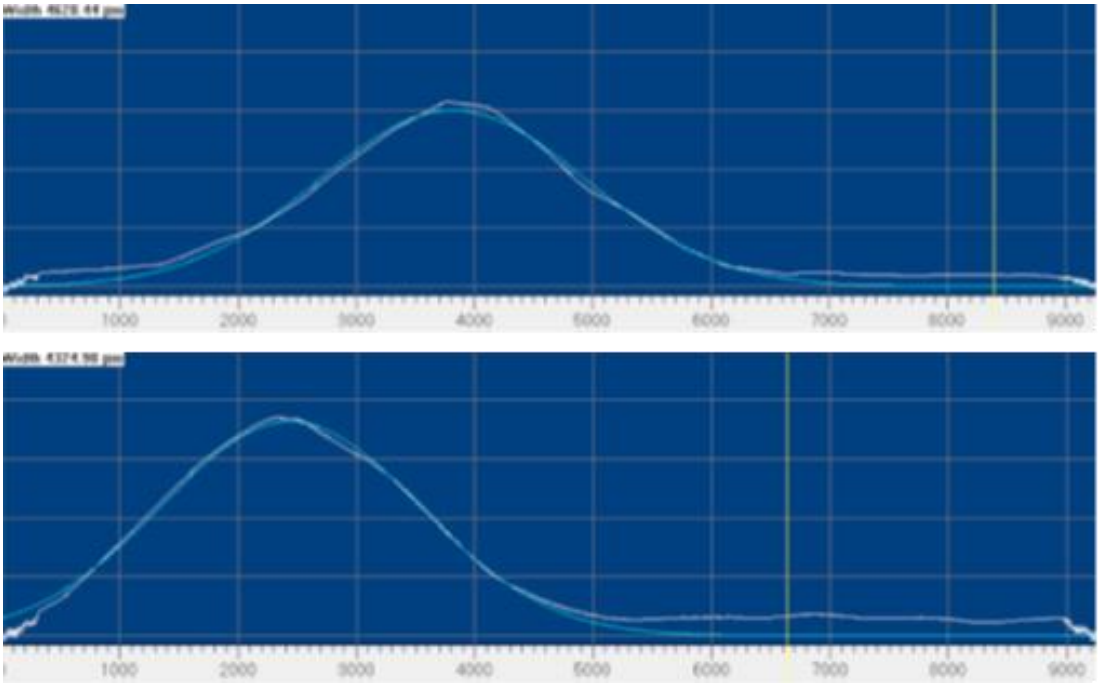

Figure 3.10. Beam Location Before Shaping (top), After Shaping (bottom)

It was eventually found that the output beam is very tolerant to slight angular misalignments and lateral shifts, and that these occurrences have no influence on the direction of the output beam. The only effect of a misalignment on the output beam is the structure of the beam itself. For a lateral shift, the intensity profile is shifted within the beam, and for an angular misalignment the profile is skewed (Figure 3.11). After contacting the manufacturer of the Focal-πShaper, it was found that the design of the beam shaper includes a tolerance in the beam deviation angle of ±5 mrad. It was assured however that these deflection angles in no way affect the intensity distribution of the beam itself.

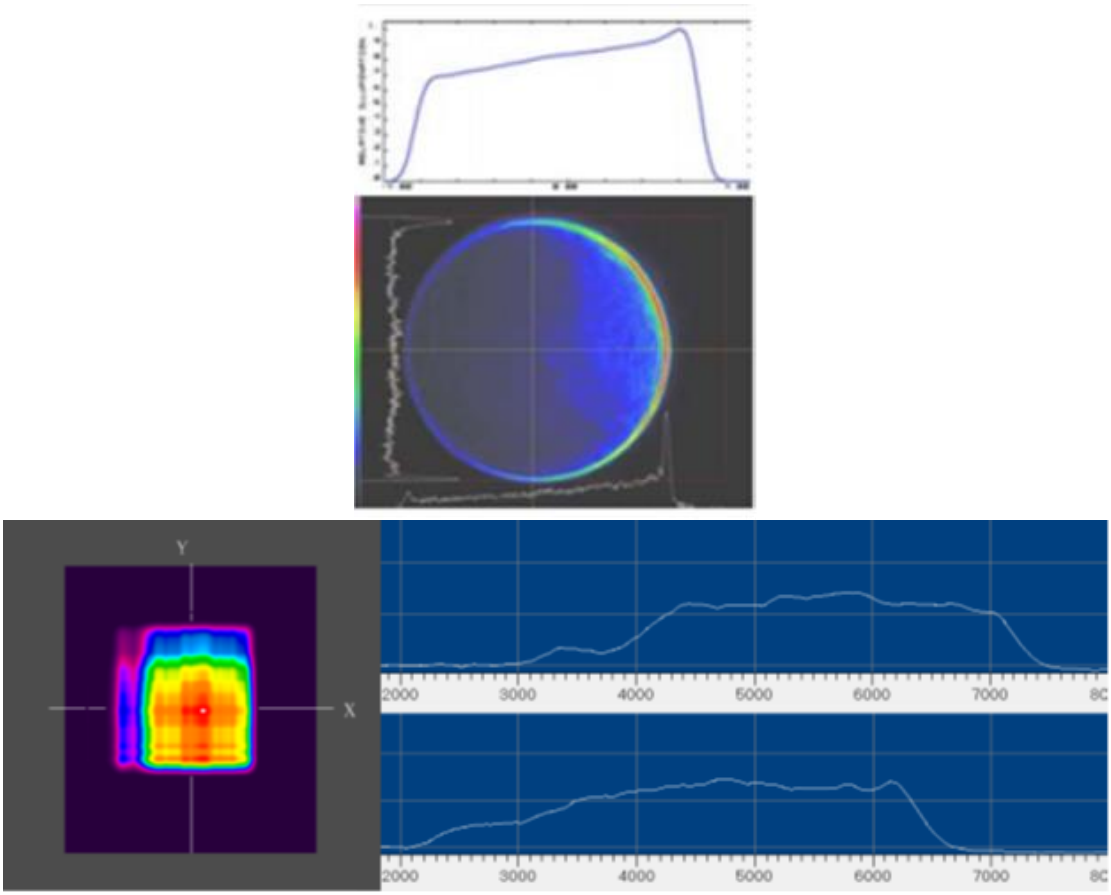

Figure 3.11. Theoretical Model of Intensity Distribution in Beam with Misaligned Beam (top), Experimental Profile of Misaligned Beam (bottom)

It seems likely therefore that the observed deviation between experimental and theoretical intensity distributions may be the result of an insufficient beam profiler, and to a lesser degree the difference in beam diameter between experimental and theoretical input beams. However, the intensity profiles observed often reflect the design principle of field-mapping; radial magnification of rays with a greater magnification of high intensity rays along optical axis. Figure 3.12 compares a beam before and after shaping. It is clear from these profiles that the intensity along the optical axis is being expanded to create a more uniform intensity distribution.

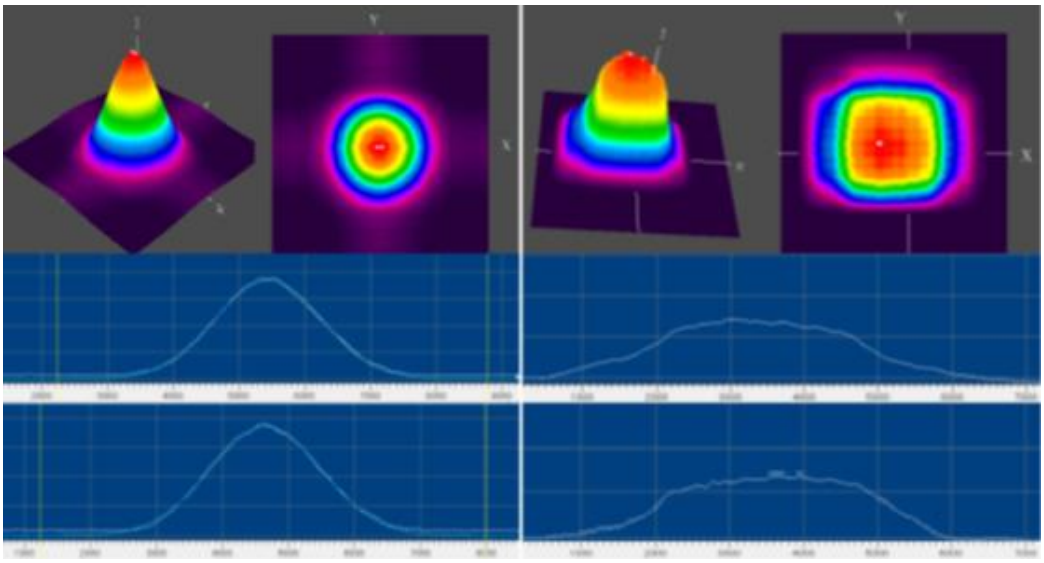

Figure 3.12. Comparison of Unshaped Beam (left), Shaped Beam (right)

The profiles measured and displayed in figure 3.12 are further corroborated by scorch marks made on photoreactive paper by a beam at the same location, with and without being shaped (Fig 3.13). It is clear from these burns that the shaped beam exhibits a large region of quasi-uniform intensity, while the unshaped beam has a high-energy concentration near the tip of the Gaussian profile.

It was then desired to scan soda-lime glass filaments with the CO_2 laser to identify how the shaped beam depicted in figure 3.12 affects the deposition process. It was found that for filaments with a 1mm diameter, the unshaped Gaussian beam requires a minimum of 3.7 W (720℃ melt pool temperature) to successfully deposit the glass filament without failure onto a soda-lime substrate preheated to 450℃. In comparison, it was found that with a shaped beam the minimum laser power required dropped to 3.1 W, with a melt pool temperature of 660℃. This indicates that shaping the beam to create a quasi-uniform intensity distribution reduces the power required for a successful soda-lime filament deposition by ~16% for 1mm diameter filaments. While there was no re-boil

observed in either process, the track scanned with a quasi-uniform intensity beam has a subjectively smoother surface (Figure 3.14).

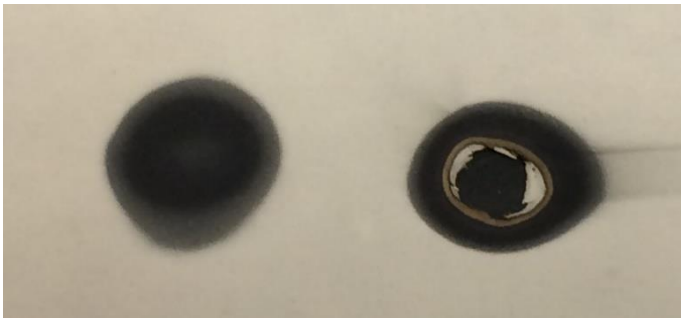

Figure 3.13. Scorch Marks on Photoreactive Beam of Shaped Beam (left), Unshaped Beam (right)

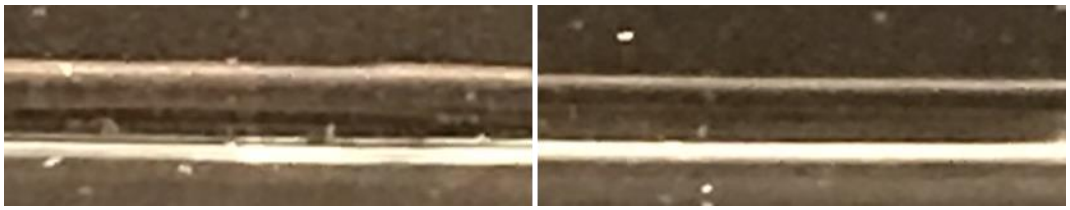

Figure 3.14. Single Track Scans of 1 mm Diameter Soda-Lime Filaments with Gaussian Beam (left), Shaped Beam (right)

Track scans were also scanned with 2mm diameter soda-lime filaments (Fig 3.15), where the greater volume of material to be softened requires a larger laser power. With these filaments, a laser power of 6 W (840ºC melt pool) is required to successfully deposit the soda-lime with a Gaussian beam, while the shaped beam requires only 5 W (810ºC melt pool). Once again, the shaping of the beam to a quasi-uniform intensity distribution reduces the laser power required by 16%. While these tracks also did not exhibit any re-boil phenomena, the conclusion that the transformation of a beam's

intensity distribution from Gaussian to flattop reduces the minimum laser power required to successfully deposit soda-lime glass filaments is further corroborated.

Figure 3.15. Single Track Scans of 2mm Diameter Soda-Lime Filaments with Gaussian Beam (left), Shaped Beam (right)

Lastly, it was attempted to scan 2mm diameter borosilicate filaments with the CO_2 laser to investigate if the shaped beam was capable of preventing re-boil within the deposited glass. Two scans were conducted: the first with a Gaussian beam and the second with a quasi-uniform intensity beam. At a laser power of 35 W, corresponding to an average melt pool temperature of 1400℃, the track scanned with a Gaussian beam clearly has several bubbles present, while the shaped beam does not (Fig 3.16). This finding supports the hypothesis that bubble formation in deposited glass may be prevented using a uniform intensity distribution laser beam.

Figure 3.16. Borosilicate Track Scanned with Gaussian Beam (left), Quasi-Uniform Intensity Beam (right)

This work endeavored to transform the intensity profile of a TEM_{00} laser beam with the field-mapping beam shaper, Focal-πShaper. While this device is capable of providing various intensity distribution transformations, it is difficult to ascertain whether or not the profiles measured near the focal plane of the shaped beam correspond to theoretical predictions. Measurements conducted away from the focal plane do exhibit many unique intensity profile distributions, but the correlation between experimental and theoretical profiles is weak at best. This weak correlation may be due issues with the scanning-head beam profiler used, or the fact the beam shaped in this work was slightly larger than the beam diameter specified in the theoretical model. Nevertheless, the primary goal for this work was to establish a beam transformation which created a more uniform intensity distribution. Beam profiles and scorch marks of a shaped beam do exhibit a radial magnification of rays along the optical axis of the beam shaper, meaning that it is possible to perform a beam transformation of a TEM_{00} laser to achieve the desired quasi-uniform intensity distribution while conserving the beam's energy.

4. FIBER-FED LASER-HEATED ADDITIVE MANUFACTURING OF GLASS

4.1. LASER-HEATED EXPERIMENTAL SETUP

The experimental platform used in this study (Figure 4.1) utilizes a CW CO_2 laser (Synrad Evolution 125, λ_0=10.6 μm, 140 μm spot size) which is incident on a soda-lime substrate. The substrate is fixed to a heater capable of reaching temperatures of 650°C, which is utilized to prevent thermal shock during the deposition process. The heater and substrate are in turn attached to a set of x-y-z stages, where the x and y stages (Aerotech ANT130-160XY) realize the horizontal movements, and a z stage (Aerotech ATS100-150) is used to move the platform upwards and downwards. A rotational stage (Aerotech ANT130-360-R) was installed on top of the x-y-z stages to enable rotations of the substrate. The fiber was fed into the melt pool (intersection of laser beam and substrate) by a custom-designed fiber feeder. 1% of the laser energy is reflected into a thermopile type power meter (Ophir 10A-V1) so that the laser power at the printing surface may be determined.

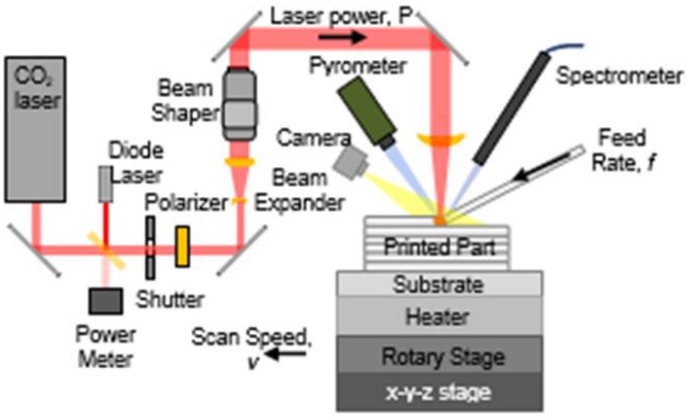

Figure 4.1. Schematic of Experimental Platform

Incandescent light is emitted from the melt pool during the printing process, with the spectrum of the radiation being dependent on the temperature of the melted glass. This incandescent emission is collected using an OceanOptics USB-4000 fiber-coupled spectrometer (calibrated with an OceanOptics LS-1-CA 2800 K light source) which has a 0.8 mm diameter interrogation region centered on the laser heated area. The process parameters investigated in this study for their effect on the deposited glass are specified to be the laser power, *P*, fiber feed rate, *f*, and the platform scan speed, *v* (Figure 4.2). The latter two parameters were consolidated into a dimensionless ratio of feed rate to scan speed, *f/v*.

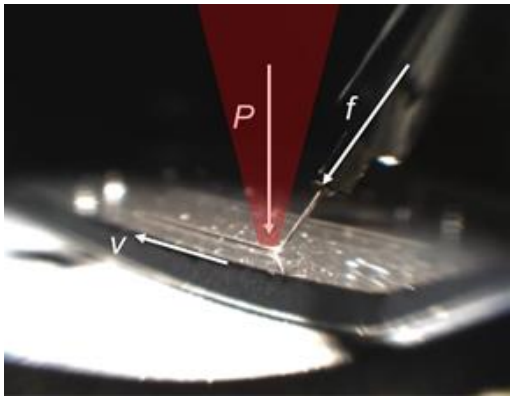

Figure 4.2. Process Parameters for Fiber-Printing Specified for Their Effect on the Deposited Glass

4.2. FIBER FEEDER DESIGN

The fiber used in this study was 100 µm soda-lime fiber provided by Schott. One of the challenges in working with this fiber involves the necessity to remove the encapsulating sizing on the fiber intended to prevent the fiber from fracturing at microcracks. Fiber stripping tools are widely available commercially, but these tools are

typically only used to remove sizing on small strips of fiber, and when it is attempted to strip the fiber continuously, these mechanical methods result in the accumulation of residual sizing particulate on the fiber itself which burn off and deposit soot, thus limiting the transmissivity of deposited glass. Dissolving the sizing by soaking the fiber in ethanol for approximately thirty minutes prior to deposition proved to be a much more efficient approach, with initial transmissivity measurements finding that the transmissivity of the deposited fiber increased from 0.54 for untreated fiber to 0.79 after an ethanol bath.

4.2.1. Hyperdermic Assembly. A significant challenge in developing a fiber-fed process is the act of feeding compliant fiber into a viscoelastic molten region. This requires a fiber feeder capable of addressing both fiber deflection and fiber buckling. To prohibit the fiber from deflecting out of the melt pool, a series of nested hypodermic tubes were used to guide the fiber from the feed wheels to the deposition site (Figure 4.3). The hyperdermic assembly is a critical component in the fiber feeder, consisting of seven nested segments of 304 Stainless steel tubes. The gauges and dimensions of these tubes are listed in Table 4.1. These tubes are available for purchase from Component Supply. These tubes are then cut into their desired lengths using a diamond cutting blade on a Dremel, after which it is very important to remove any burrs from the inner diameter of the tubing which may prevent the next inner diameter tube from being able to slide in and out. This is done using a cone single-cut bur drill bit. After selecting an appropriate size drill bit, the tip is gently inserted into both ends of the hyperdermic tube. A small amount of pressure is applied to clear any debris, after which the drill bit is removed. This is repeated for each individual tube.

Table 4.1. Gauges and Dimensions of Hyperdermic Tubes in Hyperdermic Assembly

Gauge	Inside diameter (in)	Outside Diameter (in)	Tube Length (in)
30G/Reg	0.0055/0.007	0.012/0.0125	3.5
25G/X-thin	0.0135/0.15	0.0210/0.0205	3.4
22G/X-Thin	0.0215/0.023	0.028/0.0285	3.35
19G/Thin	0.0315/0.0335	0.0415/0.0425	3.3
17G/Thin	0.0465/0.0485	0.0575/0.0585	3.15
15G/Thin	0.0595/0.0615	0.0715/0.0725	2.95
13G/Thin	0.075/0.079	0.094/0.096	2.65

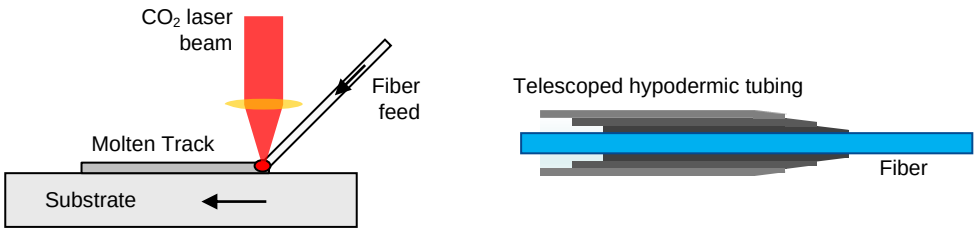

Figure 4.3. Schematic of Telescoping Hypodermic Tubing Used to Prohibit Fiber Deflection

When the tubes are nested, depending on the tolerances of the tube's diameters, it will be necessary to crimp the forward-facing ends of each hyperdermic tube (with the exception of the smallest diameter tube) to ensure that the tubes cannot move into the melt pool. The final fitting must be very tight between each tube, as any residual acrylate which is inevitably left on the quartz fiber after stripping will accumulate in the inner most diameter hyperdermic tube, creating a sufficient amount of frictions between the fiber and inside wall of the hyperdermic assembly to push the inner tubes into the melt pool. It is important that only the forward-facing side of the tubes are crimped, as it would be impossible to feed the tubing through the low-tolerance hole in the hyperdermic

assembly housing if the back end was crimped. In addition, if both ends of the tubes were crimped it would be very difficult to remove sections of the assembly for maintenance/replacement.

The hyperdermic assembly is shown fully-assembled in figure 3. The front of the assembly is the end with the smallest protruding distance of each nested tube, seen on the left end in figure 4.4. The small protrusion lengths of individual hyperdermic tubes on the forward-facing side of the assembly is critical to impart as much stiffness to the fiber feed as possible. By necessity however, the smaller diameter tubes require a slightly larger protrusion length to prevent the larger diameter tubes from blocking the quickly diverging/converging laser beam near the beam waist. The back end of the assembly, seen on the right in figure 4.4, has much larger protrusion lengths between consecutive nested hyperdermic tubes. This is done so that the innermost hyperdermic tube can reach as close as possible to the point of connection between the two 1.25” feed wheels. The consecutively larger diameter tubes are then positioned as closely as possible the diverging profiles of the feed wheels to impart the maximum amount of rigidity to the innermost tube as possible without coming into contact with the feed wheels.

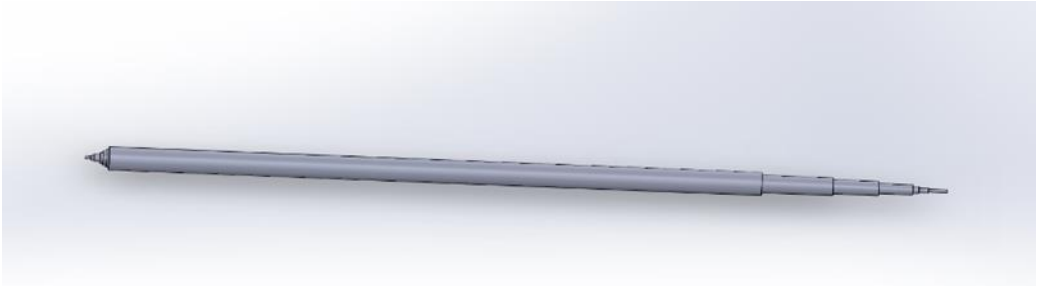

Figure 4.4. Fully Assembled Hyperdermic Assembly

When a new fiber feed is to be initialized, it is important to first remove the assembly from its housing on the fiber feeder. The fiber is then hand fed from the back of the feeder, through the wheels which are held open, and then through the empty hyperdermic assembly housing. The fiber, now protruding from the front of the feeder by several inches, is then hand fed through the back of the hyperdermic assembly. The assembly is then backed into the assembly housing and locked in place with set screws. The desired amount of fiber protrusion out the front of the hyperdermic assembly is then achieved using the jog function in the control program.

4.2.2. Feeder Body. The design of the fiber feeder is shown in Figure 4.5. A rear hyperdermic tube (17G gauge) is used to guide the fiber feed between two wheels, the drive wheel and the slave wheel. The drive wheel is connected to a Yaskawa motor which is secured to the rear of the feeder, while the slave wheel is pressed tightly against the drive wheel via two springs. The slave wheel is also wrapped with a rubber band to increase the friction between the two wheels, therefore preventing any slipping. The fiber is fed through the two wheels, after which it enters the hyperdermic assembly which is secured parallel to the feed direction via set screws in the hyperdermic housing at the front of the feeder.

The issue of fiber buckling continued to manifest in the unsupported span between the point of contact of the feed wheels and the entrance to the hypodermic assembly, labeled ‘d’ in Figure 4.6. Here the fiber would buckle to such an extent as to cause it to snap, resulting in a deposition failure. It was found that this span, *d*, must be no greater than 2.4 mm in order to prevent the fiber from buckling. With these issues addressed, a continuous fiber deposition was enabled.

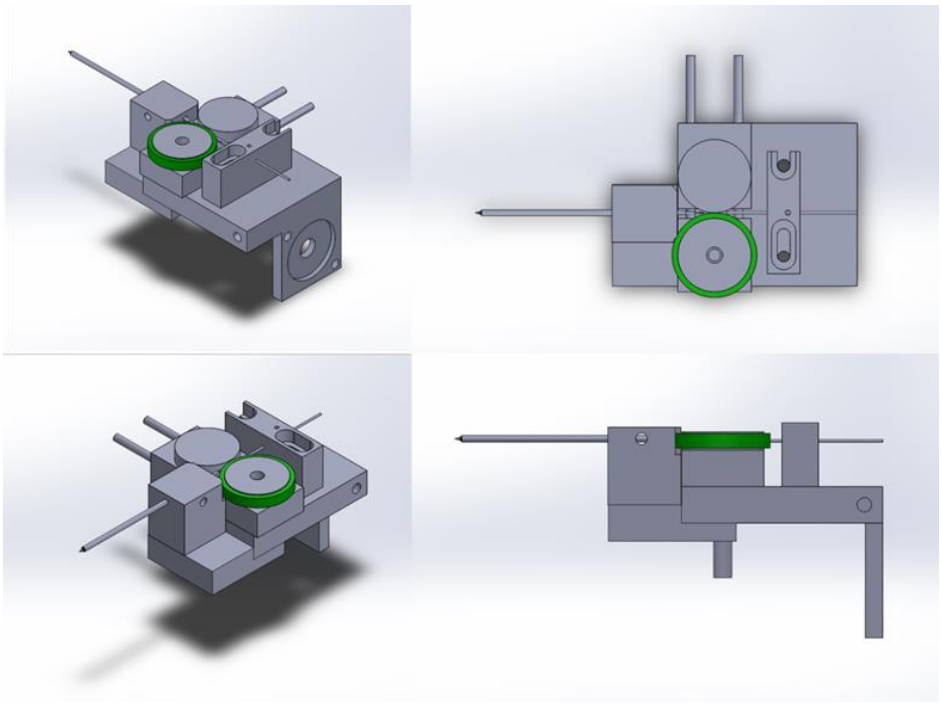

Figure 4.5. Fiber Feeder Body Design

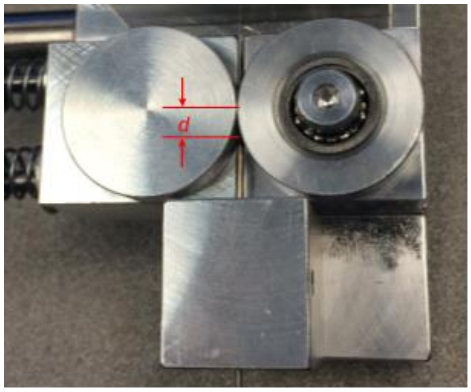

Figure 4.6. Fiber Feeder with Span, d, Identified as Critical Parameter to Prevent Fiber Buckling

4.3. SODA-LIME FIBER DEPOSITION

The fiber used in this study was 100 µm soda-lime fiber provided by Schott. One of the challenges in working with this fiber involves the necessity to remove the encapsulating sizing on the fiber intended to prevent the fiber from fracturing at

microcracks. Fiber stripping tools are widely available commercially, but these tools are typically only used to remove sizing on small strips of fiber, and when it is attempted to strip the fiber continuously, these mechanical methods result in the accumulation of residual sizing particulate on the fiber itself which burn off and deposit soot, thus limiting the transmissivity of deposited glass. Dissolving the sizing by soaking the fiber in ethanol for approximately thirty minutes prior to deposition proved to be a much more efficient approach, with initial transmissivity measurements finding that the transmissivity of the deposited fiber increased from 0.54 for untreated fiber to 0.79 after an ethanol bath.

4.3.1. Track Morphology. The process parameters *P* and *f/v* were first studied to identify their effects on the morphology of single tracks. Single tracks were deposited therefore over a range of parametric combinations of *P* and *f/v*, after which these tracks were cut and their cross sections polished. The track dimensions of height, *h*, width, *w*, and contact angle, θ, were then measured from these polished cross sections (Figure 4.7).

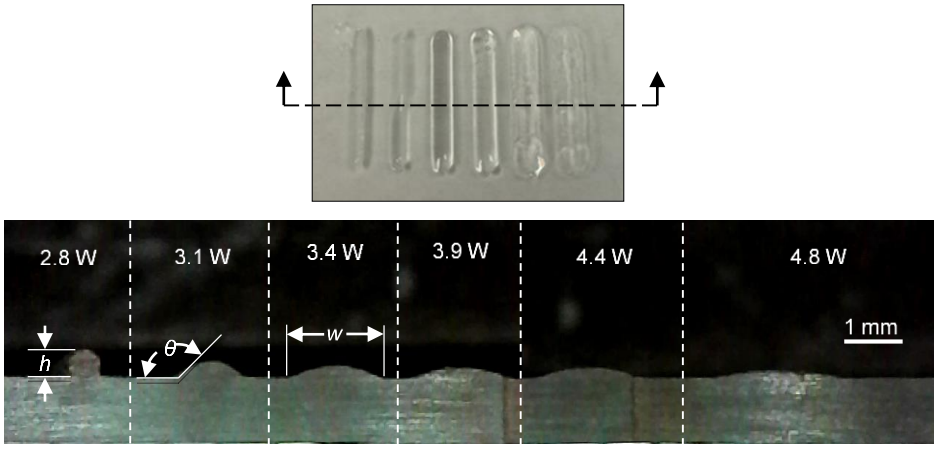

Figure 4.7. Cross Section of Single Tracks with Measured Dimensions Labeled

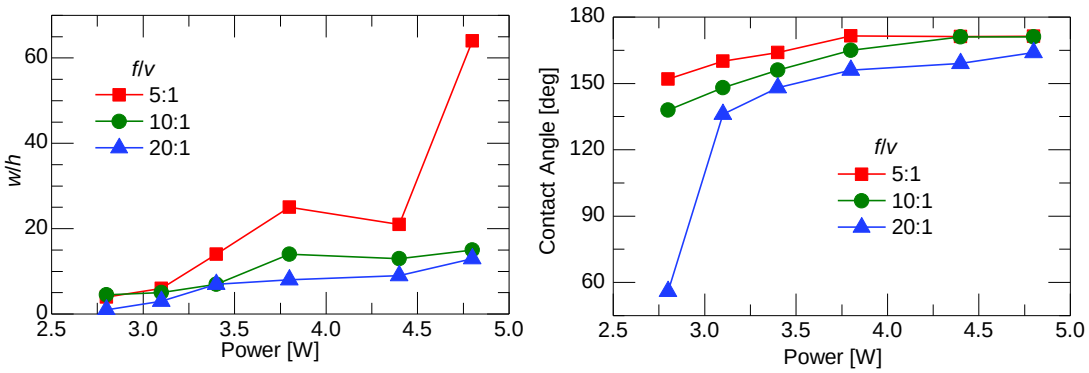

Figure 4.8. Recorded Dimensions of Single Track Morphology as s Function of Process Parameters

4.3.2. Transmissivity Measurements. The dimensions recorded of single track morphologies (Figure 4.8) were then utilized to determine appropriate step sizes for depositing 2D walls, consisting of several stacked single tracks. These walls were deposited at representative parametric combinations of *f/v* and *P*. After deposition, these walls were polished on both sides to create transmissivity samples (Figure 4.9).

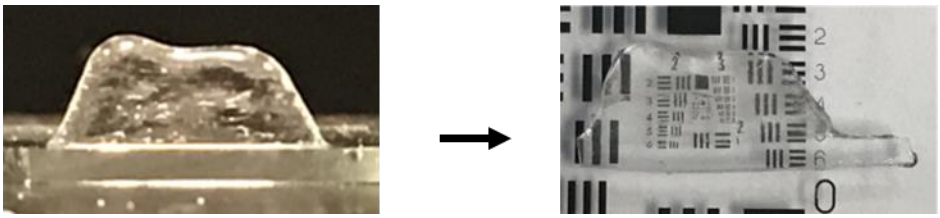

Figure 4.9. 2D Wall Post-Deposition (left), After Polishing to Create Transmissivity Sample (right)

Figure 4.10. Schematic of Transmissivity Measurement Setup

The transmissivity of these polished sample were measured at a wavelength λ = 632.8 nm with a HeNe laser and a Newport power meter (1935-C). This was done by measuring the power of the HeNe laser beam unobstructed, then re-measuring the power of the beam after it is transmitted through a sample. It was found that the transmissivity trend of the deposited fiber was parabolic (Figure 4.11). At lower laser powers, the fiber is softened and coils along the track, scattering any incident light and subsequently lowering the deposited part's transmissivity. At excessive laser powers, the soda-lime breaks down and is vaporized, depositing soot on the part which also lowers transmissivity. Between these two extreme cases however, a maximum transmissivity of 0.92 is measured for f/v = 15 and P = 6 W. This transmissivity value is ~93% of the transmissivity of conventionally manufactured soda-lime glass [30].

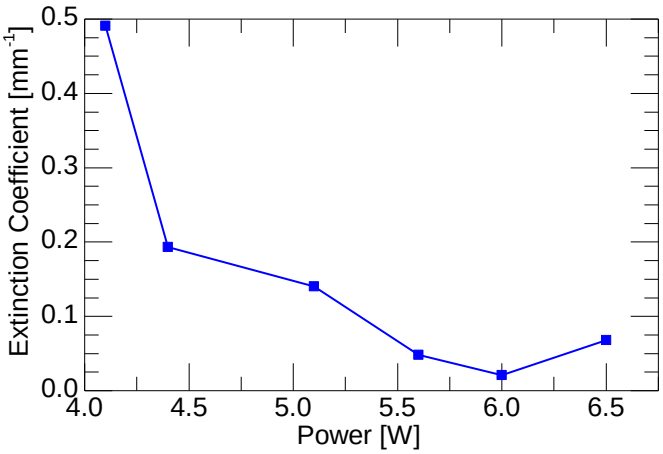

Figure 4.11. Measured Extinction Coefficient of Deposited Fiber Versus Laser Power

4.3.3. Lens Deposition. After determining the process parameters which result in the maximum transmissivity of the deposited soda-lime fiber, it was then attempted to deposit a simple lens with the fiber (Figure 4.12). The lens was printed in a single

continuous spiral deposition from the center outwards, with a constant *f/v* to create a convex profile.

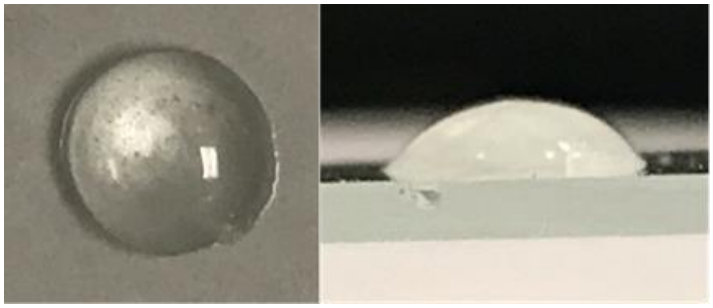

Figure 4.12. Simple Lens Printed with Soda-Lime Fiber Post-Deposition: Top View (left), Side View (right)

A large spot size (3 mm diameter) was used to reflow rings of the spiral during the deposition process to smoothen the lens surface; this reflow process however demonstrated a propensity for entrapping bubbles within the lens. Never the less, these simple printed lenses demonstrate the ability to optically focus light (Figure 4.13).

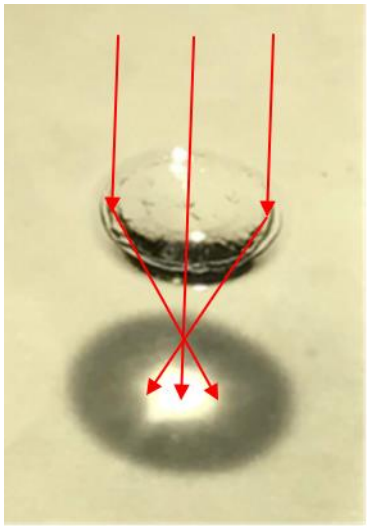

Figure 4.13. Printed Lens Post-Deposition Demonstrating Ability to Focus Light

4.3.4. Two-Dimensional Patterns. Soda-lime fiber may also be used to deposit intricate two-dimensional patterns with a high degree of dimensional accuracy (Figure 4.14). By creating SolidWorks files and importing these files into a slicer program, complicated path planning may be generated in G-code. In addition to simply outlining a desired shape, the fiber may also be used to fill in geometries through a combination of concentric perimeters and hatching (Figure 4.15).

Figure 4.14. Path Generated to Deposit S&T Cog (left) Deposited Soda-Lime S&T Cog Pattern (right)

The soda-lime fiber may also be doped with Eu_2O_3 to create patterns which fluoresce when illuminated with light at $\lambda = 405nm$ (Figures 4.16, 4.17). After reflowing the pattern with a defocused CO2 laser beam, it is found that the Eu_2O_3 still fluoresces under a blacklight.

Figure 4.15. Deposition Path Generated for ‘Joe Miner’ Profile (left), Pattern Post-Deposition (middle), Pattern Fluorescing Under λ = 405 nm Light (right)

Figure 4.16. S&T Logo Outlined with Fiber (top left) Filled S&T Logo Prior to Reflowing (bottom) S&T Logo Fluorescing Under a Blacklight Post Reflowing (top right)

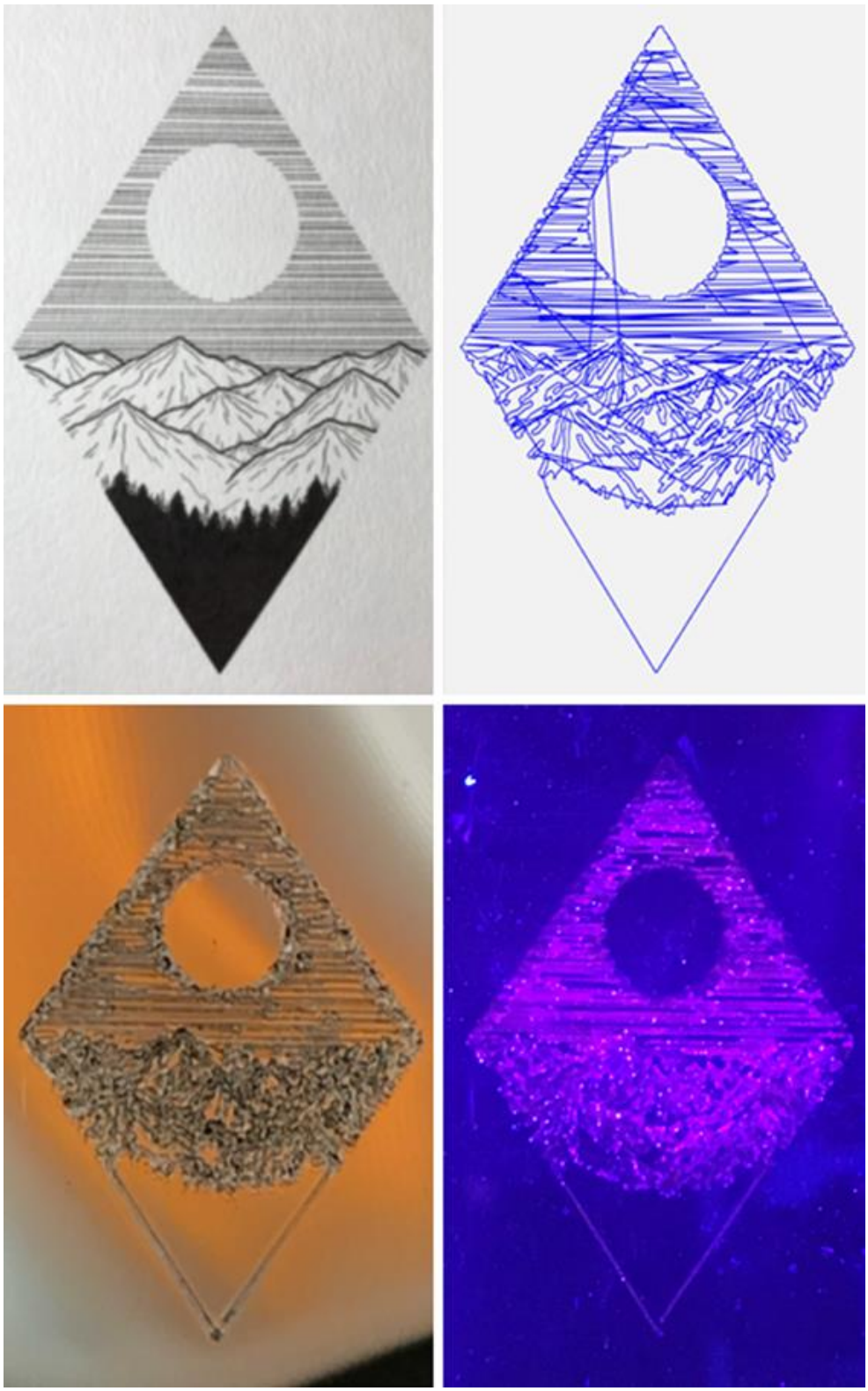

Figure 4.17. Artwork Desired to be Deposited (top left), Path Generated for Deposition (top right), Pattern Post-Deposition (bottom left), Pattern Fluorescing Under $\lambda = 405$ nm Light (bottom right)

4.3.5. Three-Dimensional Parts. In addition to depositing lenses and two-dimensional patterns, the fiber-fed laser-melted process has been found to be capable of depositing complex free-standing 3D structures such as the spiral shown in figure 4.18. These types of deposition are enabled by the temperature-dependent viscosity of soda-lime glass. As the deposited fiber is moved away from the melt pool, it cools and the viscosity quickly increases, resulting in the structure becoming very rigid. There are several conditions however which must be maintained to ensure a successful deposition: In order to prevent the failure mode of 'remelt', wherein the laser softens a previously deposited structure causing it to collapse, the melt pool must be located at the focal point of the laser. In addition, an appropriate laser power must be used to ensure that the laser energy is completely absorbed by the melting fiber, and not allowed to continue beyond the deposition site and subsequently soften any preexisting structures beneath. Free-standing structures may also be deposited with a *f/v* ratio of 1, such as the truss walls depicted in figure 4.19.

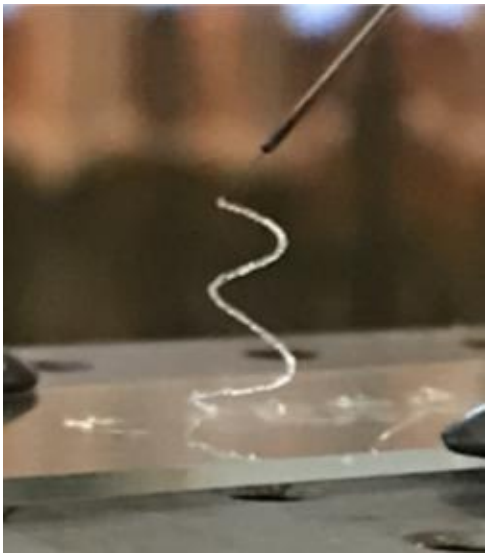

Figure 4.18. Free-Standing Spiral Deposited with Fiber-Fed Process

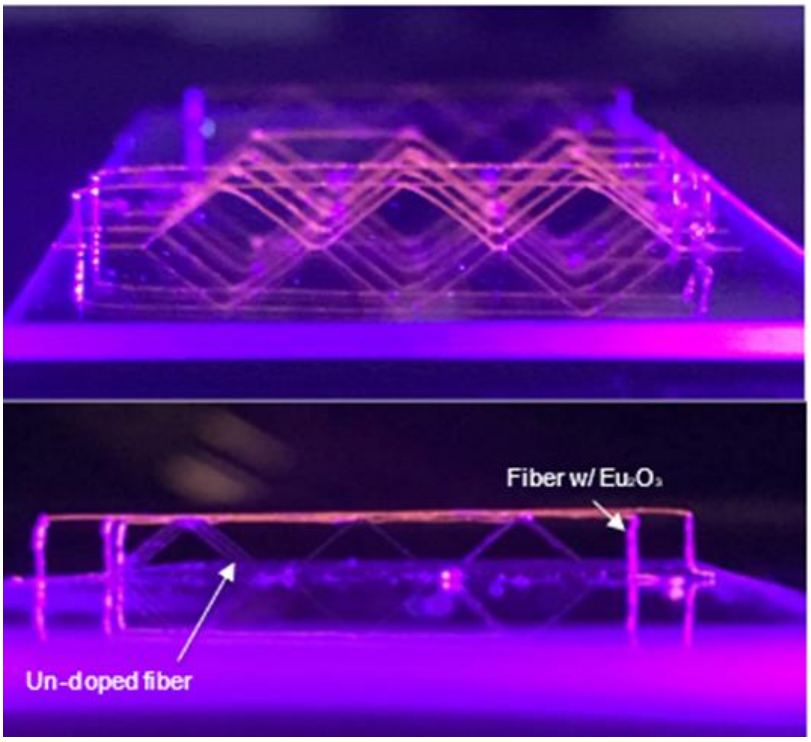

Figure 4.19. A-Frame Truss Walls Deposited Entirely with Eu2O3 Fiber (top) A-Frame Truss Walls Deposited with Soda-Lime Fiber Both Doped and Un-Doped with Eu2O3 (bottom)

4.4. QUARTZ FIBER DEPOSITION

The feedstock used in the following experiments was SMF-28 optical fiber manufactured by Corning. This fiber has an acrylic coating which is mechanically stripped following a two-hour soak in denatured alcohol, leaving a cladded quartz core which has an outer diameter of 125 µm. The cladding has a refractive index of 1.44681, while the 9 µm diameter core has a refractive index of 1.45205.

4.4.1. Single Track Morphology. Single tracks of quartz fiber were deposited at various laser powers ranging from 9.7 W to 18 W, after which the printed tracks were cross-sectioned, and their interfaces polished. The profiles of each track were then studied under a microscope with 2.5× magnification (Figure 4.20). Following inspection, the morphology of these singe tracks was able to be divided into four regimes: a) under

melted, b) continuous, c) weak vaporization, and d) strong vaporization. When the track is under melted, the laser energy is insufficient to fully melt the fiber, and the contact angle, θ, defined as the angle made between the substrate and the edge of the deposited fiber's profile, is less than 90°. However, when the contact angle is greater than 90°, the quartz fiber has melted enough to become sufficiently adhered to the substrate, creating a continuous track. As the laser power is further increased, the contact angle continues to grow as the track melts and spreads across the substrate. In addition, this weakly vaporized track is veiled in a thin layer of soot, indicating that the laser power is high enough to begin to vaporize the quartz fiber. Finally, as the laser power is further increased, the amount of vaporization increases to such a point that material is removed from the substrate, creating the negative rate of material deposition which is characteristic of the strong vaporization regime.

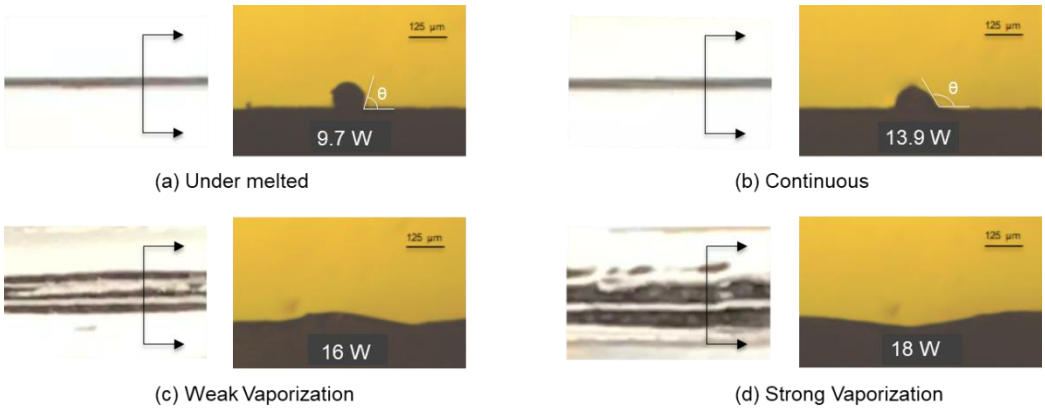

Figure 4.20. Regimes of Single Track Fiber Deposition

4.4.2. Monolayers. By printing several tracks side-by-side with a constant spacing distance between them, a monolayer may be created. Several monolayers were

deposited therefore with constant spacing distances ranging from 75 µm to 225 µm, in order to identify which distance results in the most uniform monolayer profile. These monolayers (Figure 4.21) indicate that with track spacings ≤125 µm, the deposited fiber slightly overlaps the adjacent track, preventing the fiber from adhering directly to the substrate and creating ridges which run along the length of the monolayer. When the track spacing is ≥175 µm, the fiber flows radially across the substrate and creates valleys between adjacent tracks. However, when the track spacing is set at 150 µm the deposited fiber is appropriately constrained, ensuring that the molten glass flows evenly to create a monolayer with a sufficiently uniform height.

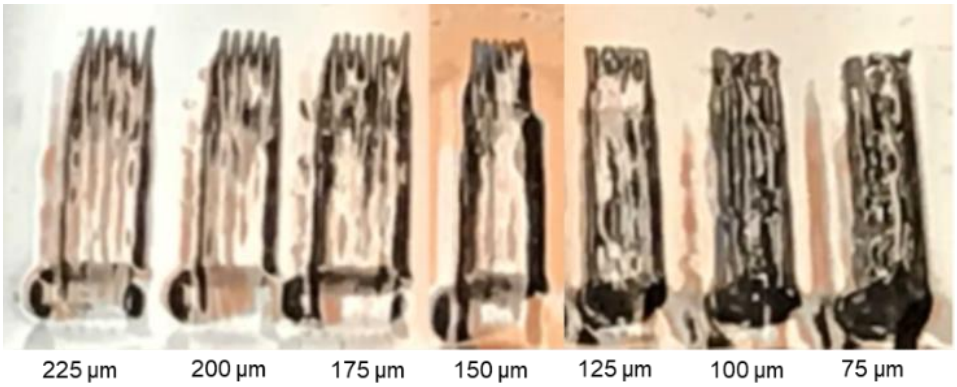

Figure 4.21. Monolayers Deposited with Various Track Spacings

4.4.3. Transmissivity Measurements. The monolayer deposition approach with a constant track spacing of 150 µm was then utilized to deposit walls for subsequent transmissivity measurements. Nine walls with dimensions 5×0.5×2 mm were printed, with each layer of the wall consisting of a monolayer comprised of three single tracks (Figure 4.22).

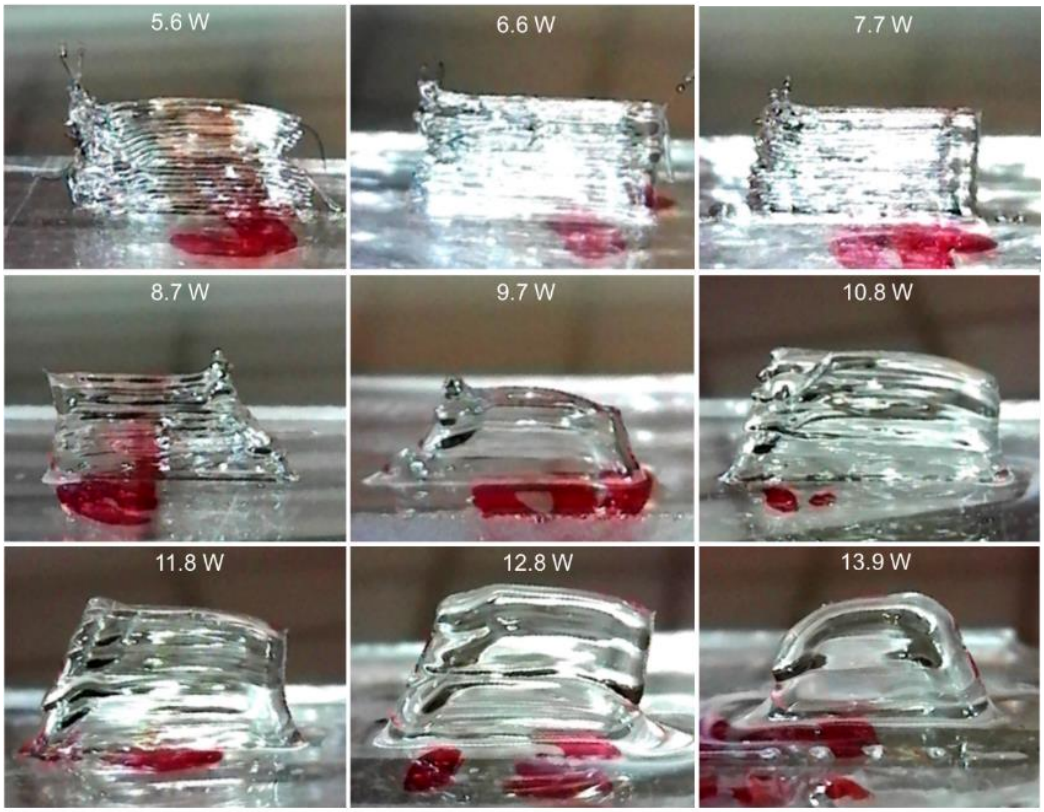

Figure 4.22. Walls Deposited with Quartz Fiber for Transmissivity Measurement

The transmissivity of these samples was then measured with a HeNe laser (λ = 632.8 nm) and a Newport power meter Model 1935-C. These measurements, plotted in Figure 4.23, depict an interesting trend. At lower laser powers, ranging from 5.6–8.7 W, the transmissivity only reaches a maximum value of 0.502. However as the power is increased to 9.7 W, the transmissivity drastically jumps to 0.874, increases to a maximum value of 0.884 at a power of 10.8 W, and then decreases with further increasing laser power. The consistently low transmissivity observed in samples printed at lower laser powers is likely due to inclusions present between adjacent tracks. As stated earlier, tracks deposited with laser powers lower than 9.7 W are characterized as under melted, meaning that there are large voids between adjacent tracks in each monolayer of the wall.

Air has a different refractive index than quartz, so light is scattered as it moves from one medium to the next, which likely accounts for the consistently low transmissivities measured with these low-power walls.

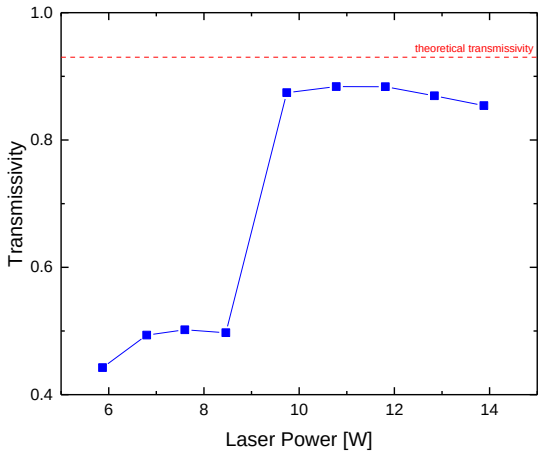

Figure 4.23. Transmissivity of Quartz Walls Deposited at Various Laser Powers

The drastic jump in transmissivity observed at P= 9.7 W was speculated to result from the melt pool temperature exceeding the melting temperature of the quartz fiber. This would cause the deposited quartz to flow into the voids between adjacent tracks and therefore prohibit inclusions. To confirm this hypothesis, a pyrometer was used to take melt pool temperature measurements during monolayer depositions over the same range of laser powers (Figure 4.24). While these results indicate that the large increase in transmissivity does indeed coincide with the melt pool temperature increasing beyond the melting temperature of quartz, the focused spot size of the pyrometer is slightly smaller than the laser spot used to deposit the quartz fiber. Because the pyrometer measures the

average temperature within its spot size, the actual melt pool temperature may vary slightly from their measured values.

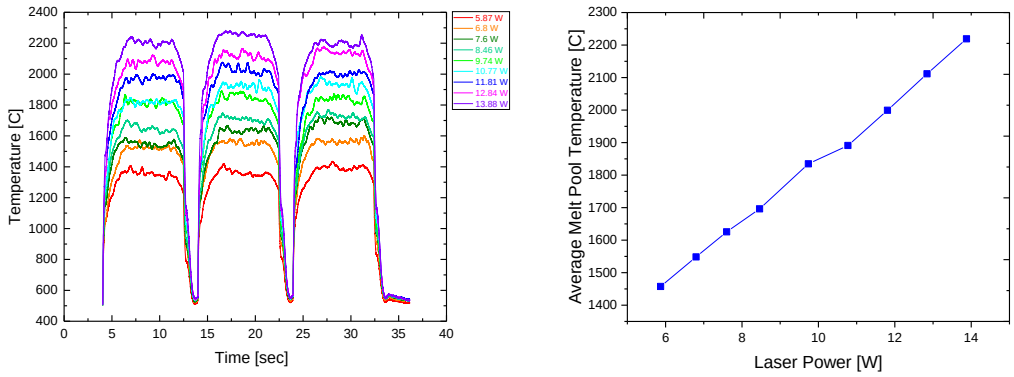

Figure 4.24. Melt Pool Temperature Data Collected During Monolayer Deposition for Various Laser Powers (left), Average Melt Pool Temperature Versus Laser Power (right)

Lastly, the gradual decrease in transmissivity in walls deposited with laser powers greater than 11.8 W was theorized to be due to the melt pool temperature exceeding the vaporization temperature of the quartz fiber. As the quartz is vaporized, more and more soot is gradually deposited on the printed structure which scatters and absorbs light, thereby limiting the sample's transmissivity. To test this hypothesis therefore, a spectrometer was utilized to measure the spectral emissions of the melt pool. The light emitted from the melt pool shows a spectral peak at a wavelength of 588.5 nm for laser powers $\geq$ 11.8 W. The onset of this peak corresponds to the vaporization of the fiber, as the quartz glass begins to break down into its constituent parts. The emergence of this spectral peak when P = 11.8 W therefore supports the hypothesis that the gradual decrease in transmissivity observed with further increasing laser powers is the result of soot deposited during the vaporization process.

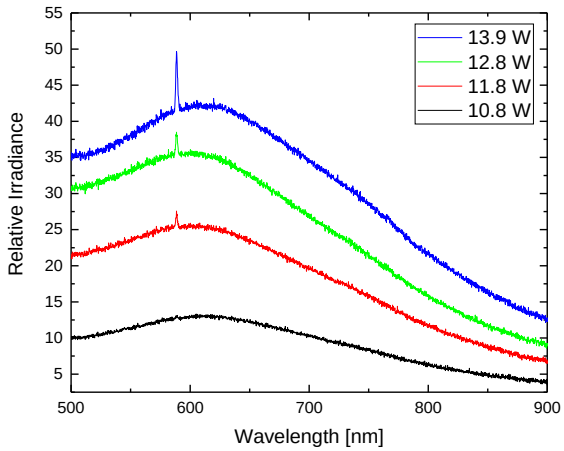

Figure 4.25. Radiation Spectra of Quartz Fiber Melt Pools Around Vaporization Threshold

With the ability of the fiber-fed process to deposit transparent parts thus proven, it was then attempted to deposit larger three-dimensional quartz structures which were likewise transparent and inclusion-free. A 3D block of quartz was deposited by stacking several monolayers consecutively on top of each other, with a track spacing of 150 µm, 50 µm step size, P=9.7 W, and f=v=1 mm/s. The resulting block, having dimensions of 3×1×1 mm is seen to be transparent and inclusion-free (Figure 4.26(a)). This block then had its upper surface polished, creating a flat window of deposited quartz (Figure 4.26(b)). This window was placed over a 1951 AFRL resolution test chart to qualitatively observe the level of refractive index homogeneity, which is an important characteristic in optical glass. It is seen in figure 4.26(c)-(d) that there is little difference in the image of the AFRL resolution chart when it is seen through the quartz window. However as the distance between the sample and pattern is increased to 10 mm, thus ensuring that light from points in the object space is passed through the entire sample before being focused onto the image plane, the image of the AFRL chart becomes slightly distorted, indicating

the presence of index inhomogeneity (Figure 4.26(e)). This inhomogeneity may be due to the slight difference in the refractive index between the cladding and the core of the deposited fiber.

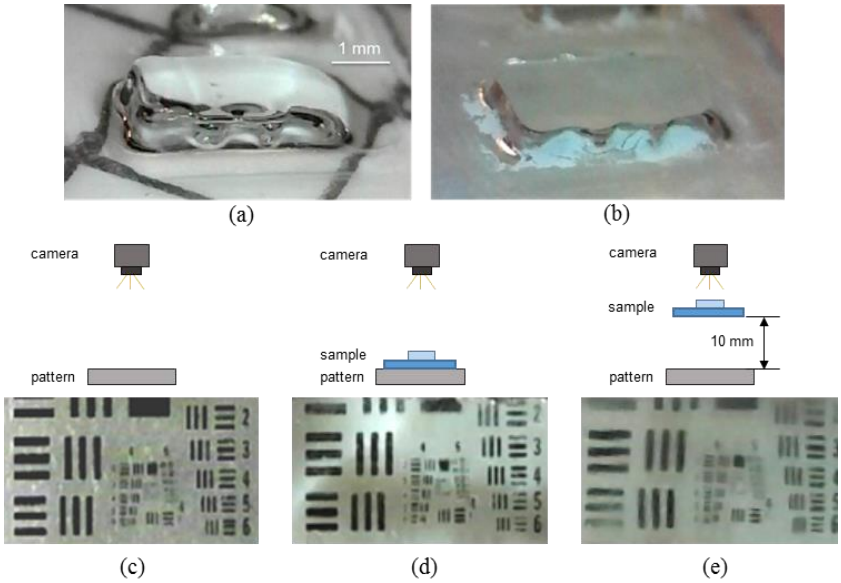

Figure 4.26. Inclusion-Free Block of Quartz Glass (3×1×1 mm) Deposited with Fiber-Fed Approach

The transmissivity of the quartz block was measured using a HeNe laser (λ = 632.8 nm) and a Newport power meter Model 1935-C, and found to have a value of 0.909. The increase in transmissivity observed for the block in comparison with a wall deposited with the same platform parameters is likely due to the difference in morphology of the structures. The block has a smooth upper surface and a flat lower surface, resulting in the transmitted HeNe beam roughly keeping its shape (Figure 4.27(b)). However, when transmitting a beam through a quartz wall, the individual fiber layers which constitute the wall act like cylindrical lenses and change the beam shape to

create long vertical lines which scatter light away from the power meter aperture (Figure 4.27(c)-(d)).

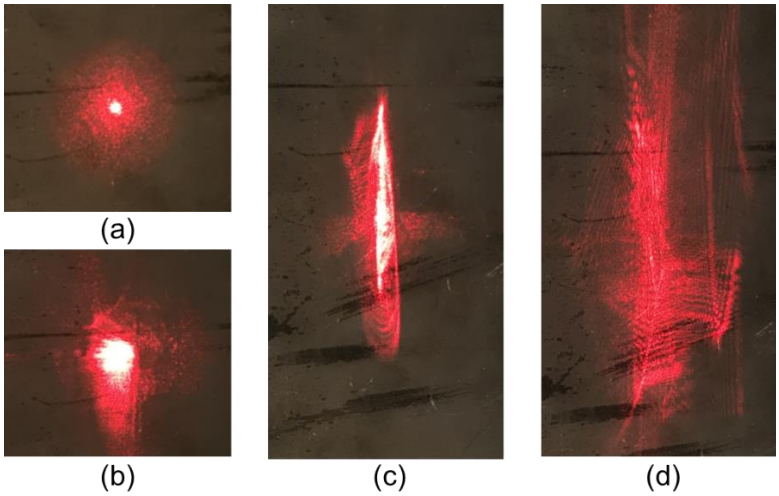

Figure 4.27. HeNe Laser Beam Incident on Wall After Transmission Through: (a) Air, (b) Printed Quartz Block, (c) Quartz Wall Printed at P = 10.8 W, and (d) Quartz Wall Printed at P = 6.6 W

4.4.4. Quartz Lens Deposition. With the ability of the fiber-fed laser-heated process to deposit transparent quartz structures now proven, it was then attempted to deposit a cylindrical lens wherein several monolayers of varying widths are stacked to create a cylindrical profile (Figure 4.28 (a)-(b)). The laser was then used to scan the deposited glass after printing monolayer, reflowing the deposited glass to create a round profile. The resulting lens shapes a transmitted HeNe laser beam into the vertical line characteristic of a cylindrical lens (Figure 4.28 (d)-(e)).

A second deposition approach was then used to create a lens where fiber was deposited in a spiral pattern, starting in the center and moving outwards with a constant angular velocity. By maintaining a constant angular velocity, the feed rate-to-scan speed

ratio decreases as the fiber is deposited further away from the center of the lens, creating the desired curvature profile (Figure 4.29). This simple lens demonstrates the ability to optically focus light, and magnifies the image of an AFRL resolution test chart (Figure 4.30). Curvature of this lens was designed to have a focal distance of 2 mm. Using the lens maker's equation (Eq. (3)), the actual focal length was determined to have a value of 2.48 mm.

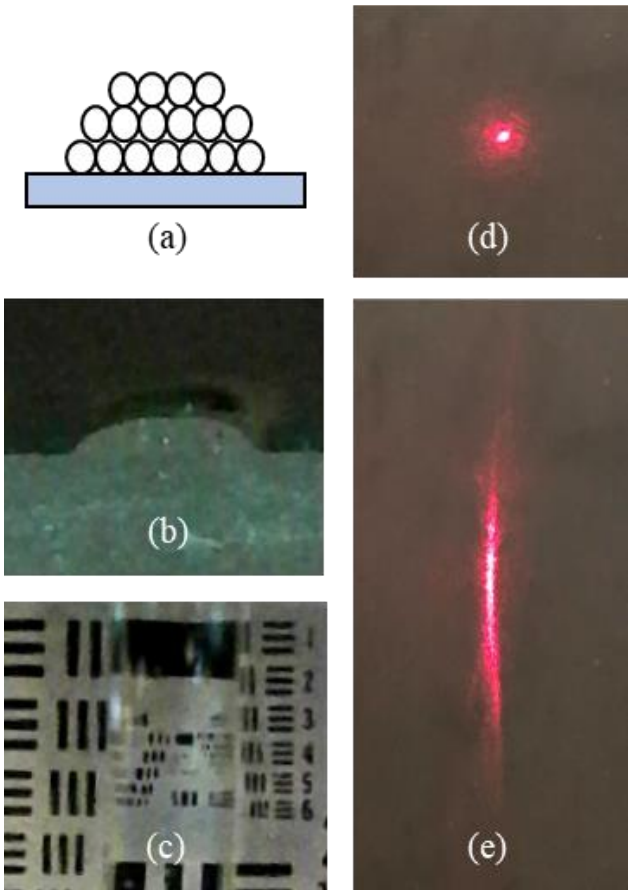

Figure 4.28. (a) Monolayer Patterns Used to Create Cylindrical Profile, (b) Polished Cross-Section of Deposited Cylindrical Lens, (c) Cylindrical Lens Imaging 1951 AFRL Resolution Test Chart, (d) Bare HeNe Laser Beam, (e) HeNe Beam Transmitted Through Cylindrical lens

$$\frac{1}{s_i}+\frac{1}{s_o}=\frac{1}{f} \tag{3}$$

This variation in the focal length from its design value is likely caused by the large spot size of the laser, which reflows the deposited glass in a manner which can be difficult to accurately predict. By changing the deposition technique to print a lens which is comprised of a series of concentric circles, and by varying the angular velocity from one ring to the next, thereby changing the ratio of feed rate to scan speed, it is believed that aspheric lenses and other more complicated lens profiles may be obtained, which more closely match their design profiles.

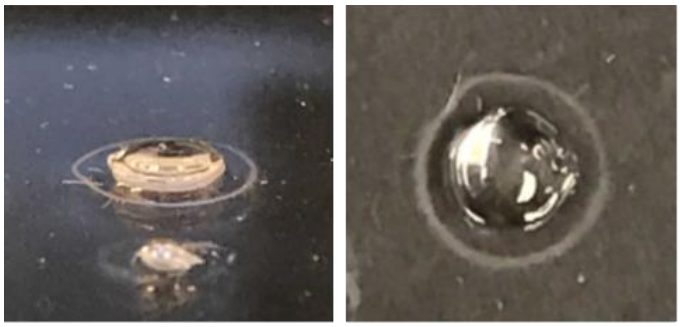

Figure 4.29. Oblique View (left) and Top-Down View (right) of Simple 3D Printed Quartz Lens

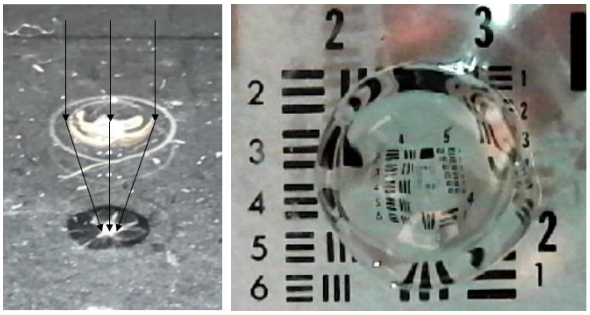

Figure 4.30. Simple Lens Optically Focusing Light (left) Imaging AFRL Resolution Test Chart (right)

A second deposition approach for spherical lenses was adopted in an attempt to improve the degree to which the profile of the spherical lenses adhered to a design profile (Figure 4.31). Each layer consists of a series of concentric circles, starting from the inside and working its way outwards. Each ring is designed to maintain a constant feed rate-to-scan speed ratio of 1:1. After depositing each layer, the CO_2 laser is then defocused, and the layer is reflowed to create a smooth layer.

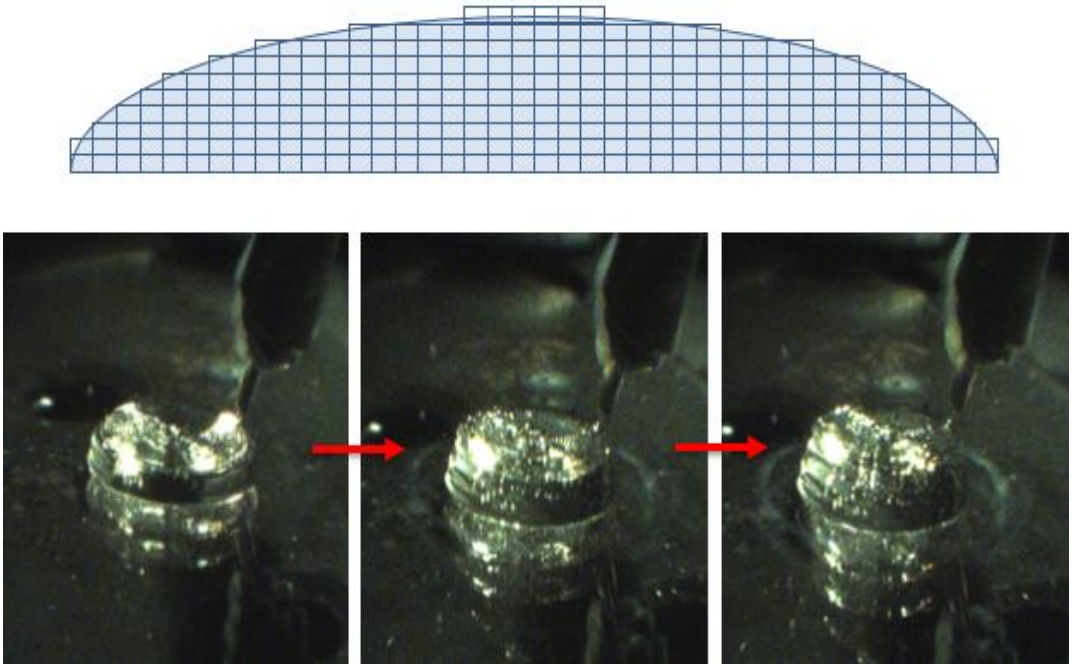

Figure 4.31. Cross-Section of Lens Profile Design (top) Progression of Lens Deposition (bottom)

It was determined that lenses deposited with a larger radius of curvature match their design profile much better than lenses with a smaller radius of curvature. When lenses are printed with a smaller radius of curvature, the sides of the lenses slump much more than intended, as the reflowed fiber attempts to consolidate into a bubble instead of retaining the edges of each layer.

Lenses deposited with Quartz SMF do an adequate job of imaging, be it the pixels on an LCD monitor, or an AFRL Resolution test chart (Figure 4.32). It is unclear at this time whether or not the quartz glass within the core is mixing with the cladding during the deposition, or if there remains segregation between the slightly higher index of refraction glass in the core, and that of the cladding. Any effects of this index inhomogeneity are soon to be measured and compared with lenses which are deposited using specially drawn quartz fiber, where the entire fiber is comprised of material with the same index of refraction.

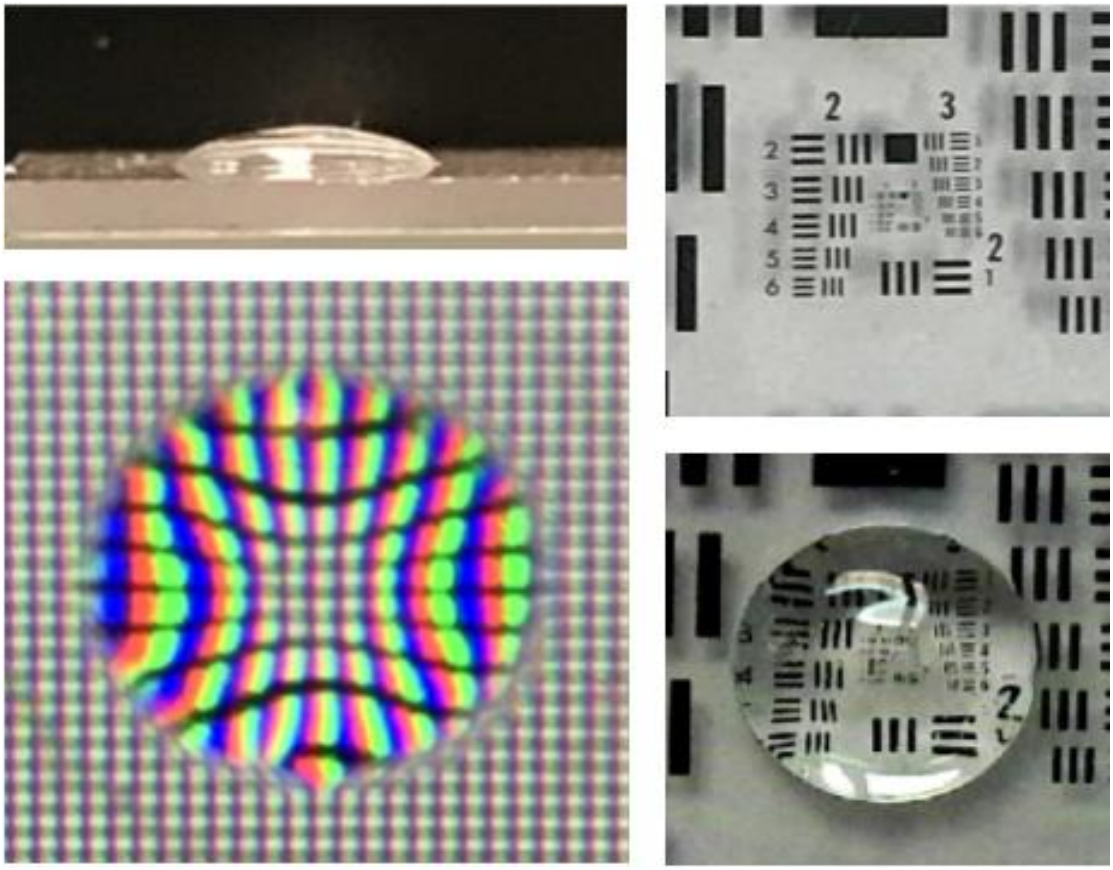

Figure 4.32. Profile of Spherical Lens (top left), Lens Imaging Pixels on LCD Monitor (bottom left), AFRL Resolution Test Chart with No Lens (top right), AFRL Resolution Test Chart Imaged Through Spherical Lens (bottom right)

4.4.5. Three-Dimensional Parts. By printing with a feed rate-to-scan speed ratio of 1:1 and a small spot size of ~200 µm, large 3D parts may be printed with quartz SMF fiber. Quartz glass is more ideal for printing larger structures, because the quartz fiber does not slump as easily as its soda-lime counterpart when subjected to laser energy on subsequent deposition passes. Simple geometries such as those depicted in figure 4.33 have been deposited with heights of up to 15 mm, and more complex geometries such as arches (Figure 4.34) have been demonstrated with parts successfully deposited up to 20 mm high. These more complex geometries have been made possible by using the same slicer program used to deconstruct the 2D patterns discussed above, however the path planning required to select the next appropriate vector when moving from one z-position to the next still often requires manual input.

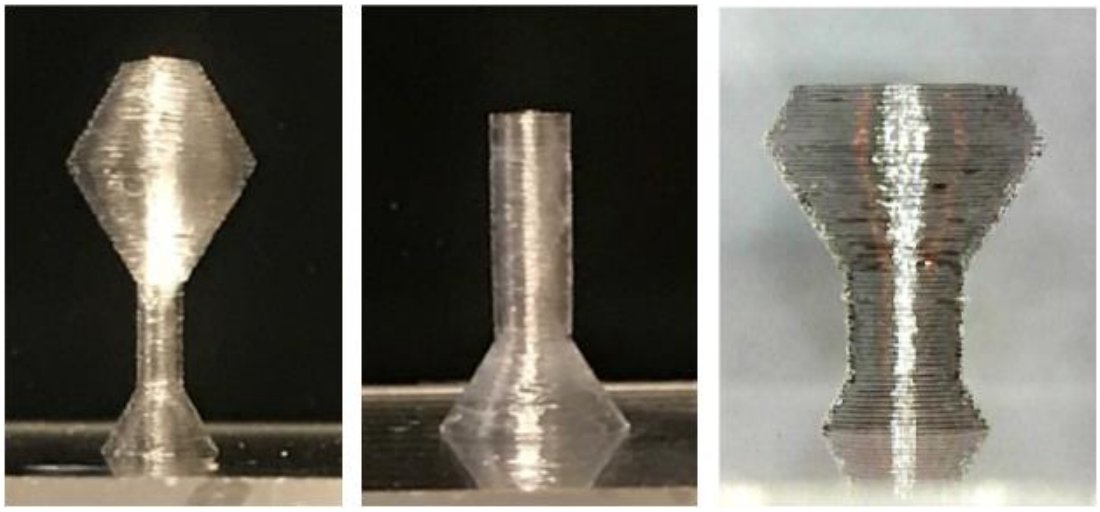

Figure 4.33. Simple Geometries Deposited with Quartz SMF

In addition to the continuous structures discussed above, more free-standing complicated geometries involving many starts and stops in the deposition have been

accomplished, such as trusses (Figure 4.35). These trusses involve the deposition of free-standing fiber in directions which are not aligned with the fiber feeder direction, a disconnect between the substrate and the fiber feeder, and a subsequent reconnection for the next sequence in the deposition. The necessity for consistent disconnects and reconnects which do not damage the already deposited structure requires the use of lead-ins and lead-outs, which often result in unnecessary segments of fiber deposited along the periphery of the truss. The possibility of adding a terminal portion to the deposition code which uses the laser to sever the connections between the intended truss structure and unnecessary segments of fiber deposited to create a lead-in or lead-out will soon be tested.

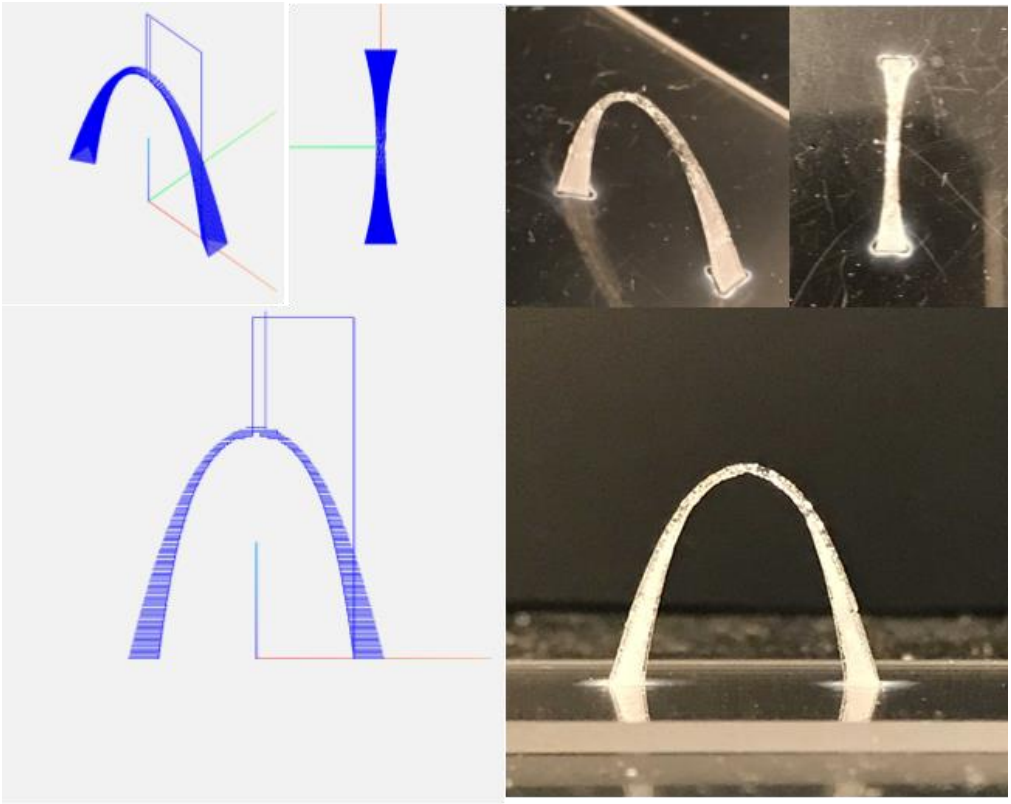

Figure 4.34. St. Louis Gateway Arch Generated Deposition Path (left) Structure Post-Deposition (right)

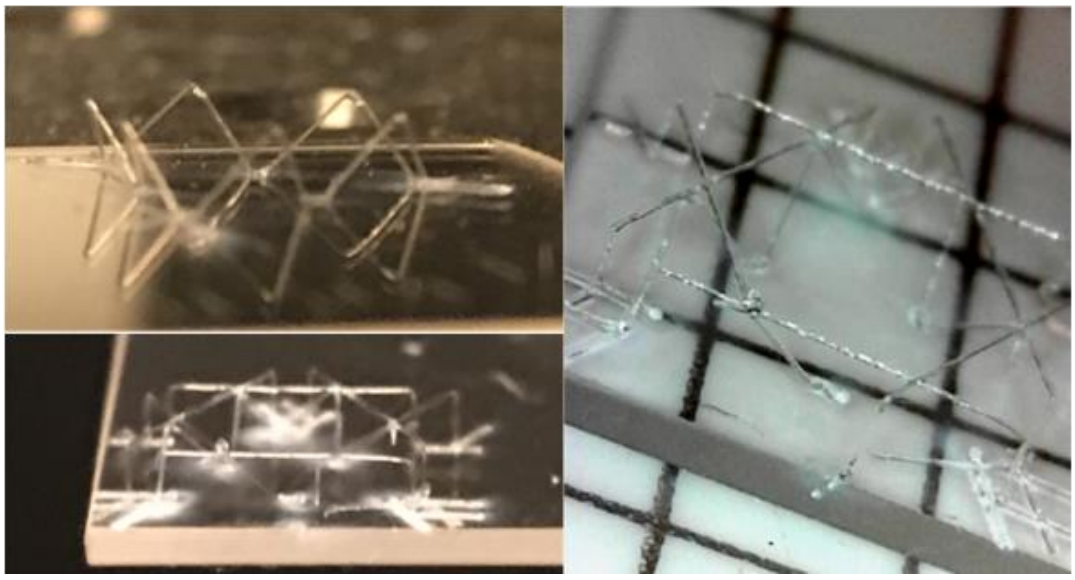

Figure 4.35. Fiber Truss in Various Stages of Deposition

In addition to depositing single segments of free-standing fiber, the 3D printing of a truss also requires the joining of two deposited segments together in certain locations. It has been found that if two segments that are intended to be joined in some location are deposited with the same height, then the fiber being deposited to join the second segment to the first will simply destroy the initial segment. Therefore, a Z-offset of 100 µm is required between two segments that are intended to be joined.

BIBLIOGRAPHY

[1] M. Fateri, A. Gebhardt, S. Thuemmler, L. Thurn, “Experimental investigation on Selective Laser Melting of Glass,” Physics Procedia, 56, 357-364 (2014).

[2] S. Kumar, “Selective Laser Sintering: A Qualitative and Objective Approach,” JOM Journal of Minerals, Metals and Materials, 55(10) 43-47 (2003).

[3] J.P. Kruth, X. Wang, T. Laoui, L. Froyen, “Lasers and materials in selective laser sintering,” Assembly Automation, 23(4) 357-371 (2003).

[4] R.S. Khmyrov, S.N. Grigoriev, A.A. Okunkova, and A.V. Gusarov, "On the Possibility of Selective Laser Melting of Quartz Glass," Physics Procedia, 56 345-356 (2014).

[5] M. Fateri, A. Gebhardt, “Selective Laser Melting of Soda-Lime Glass Powder,” Int. J. Appl. Ceram. Technol., 12(1) 53-61 (2015).

[6] J.P. Kruth, P. Mercelis, J. Van Vaerenbergh, “Binding mechanisms in selective laser sintering and selective laser melting,” Rapid Prototyping Journal, 11(1) 26-36 (2005).

[7] F. Klocke, H. Wirtz, “Selective Laser Sintering of Zirconium Silicate,” Proc. Solid Freeform Fabrication Symposium, Austin, 605-612 (1998).

[8] Ph. Bertrand, F. Bayle, C. Combe, P. Goeuriot, I. Smurov, “Ceramic components manufacturing by selective laser sintering,” Applied Surface Science, 254(4) 989-992 (2007).

[9] G. Marchelli, R. Prabhakar, D. Storti, M. Gantor, “The guide to glass 3D printing: developments, methods, diagnostics and result,” Rapid Prototyping Journal 17/3 187-194 (2011).

[10] R.S. Khmyrov, S.N. Grigoriev, A.A. Okunkova, and A.V. Gusarov, "On the Possibility of Selective Laser Melting of Quartz Glass," Physics Procedia 56 345-356 (2014).

[11] J. Hostetler et al., “Selective Laser Sintering of Low Density, Low Coefficient of Thermal Expansion Silica Parts,” Proceedings of Solid Freeform Fabrication Symposium. Austin, TX, 978-988 (2016).

[12] M. Fateri, A. Gebhardt, “Selective Laser Melting of Soda-Lime Glass Powder,” Int. J. Appl. Ceram. Technol., 12(1) 53-61 (2015).

[13] J. Luo, L.J. Gilbert, C. Qu, R. Landers, D. Bristow, and E. Kinzel, 2016, "Additive manufacturing of transparent soda-lime glass using a filament-fed process," Journal of Manufacturing Science and Engineering.

[14] Klein, J., Stern, M., Franchin, G., Kayser, M., Inamura, C., Dave, S., Weaver, J. C., Houk, P., Colombo, P., and Yang, M., 2015, "Additive manufacturing of optically transparent glass," 3D Printing and Additive Manufacturing, 2(3), pp. 92-105.

[15] http://micron3dp.com/blogs/news/34473924-breakthrough-in-3d-printing-glass (2015).

[16] https://www.corning.com/media/worldwide/coc/documents/Fiber/SMF-28%20Ultra.pdf

[17] F. Klocke, C. Ader, "Direct Laser Sintering of Ceramics," Proc. Solid Freeform Fabrication Symposium, Austin, 447-455 (2003).

[18] J.L. Song, Y.T. Li, Q.L. Deng, D.J. Hu. "Rapid prototyping manufacturing of silica sand patterns based on selective laser sintering," Journal of Materials Processing Technology 187, 614-618 (2007).

[19] Y. Tang, J.Y.H. Fuh, H.T. Loh, Y.S. Wong, L. Lu, "Direct Laser Sintering of a Silica Sand," Materials and Design 24(8) 623-629 (2003).

[20] ASTM, "Standard Test Method for Flexural Strength of Advanced Ceramics at Ambient Temperature," C1161 (2013).

[21] ASTM, "Standard Test Method for Density of Powder Metallurgy (PM) Materials Containing Less Than Two Percent Porosity," B311–13 (2013).

[22] "High efficient laser beam shaping systems," pishaper.com/shaping_system.php.

[23] A. Laskin, V. Laskin, "Controllable Beam Intensity Profile for the Tasks of Laser Material Processing," Paper 707.

[24] A. Laskin, "Achromatic Optical System for Beam Shaping," U.S. patent 8,023,206 (Sep. 20, 2011).

[25] B.R. Frieden, "Lossless conversion of a plane laser wave to a plane wave of uniform irradiance," Appl. Opt. 4, 1400-1403 (1965).

[26] J.L. Kreuzer, "Coherent light optical system yielding an output beam of desired intensity distribution at a desired equiphase surface," U.S. patent 3,476,463 (Nov. 4, 1969).

[27] P.W. Rhodes, D.L. Shealy, “Refractive optical systems for irradiance redistribution of colliated radiation: their design and analysis,” Appl. Opt. 19, 3545-3553 (1980).

[28] J.A. Hoffnagle, C.M. Jefferson, “Design and performance of a refractive optical system that converts a Gaussian to a flattop beam,” Appl. Opt., Vol. 39, No. 30, Oct 20, 2000.

[29] A. Laskin, H. Bae, V. Laskin, A. Ostrun, “Beam Shaping of Focused Beams for Microprocessing Applications,” Paper P136.

[30] M. Fateri, A. Gebhardt, “Selective Laser Melting of Soda-Lime Glass Powder,” Int. J. Appl. Ceram. Technol., 12(1) 53-61 (2015).

VITA

John Michael Hostetler grew up in Columbia, MO where he attended David H. Hickman High School. Upon graduation in 2010, he attended college at Missouri University of Science and Technology in Rolla, MO. He received Bachelors of Science in Aerospace and Mechanical Engineering and a minor in Mathematics in Spring 2016, after which he began to pursue an Masters of Science in Mechanical Engineering at Missouri University of Science and Technology with Dr. Ed Kinzel as his advisor. Upon receiving his Masters of Science in Mechanical Engineering in August 2018, he moved with his wife Madison to Houston, TX to begin his career.